University of Seville
Master in Nuclear Physics

Characterization of scintillators for ion detection diagnostics in nuclear fusion reactors

Micaela Videla Trevin
November 2021

Supervisors:
Eleonora Viezzer
Javier Ferrer Fernández

Departamento de Física Atómica, Molecular y Nuclear
Facultad de Física

Plasma Science and Fusion Technology
Centro Nacional de Aceleradores

Abstract

Scintillator materials are used for ion detection diagnostics in nuclear fusion devices. These diagnostics obtain information from the plasma in a fusion device, for example, in a tokamak. Scintillators working principle is based on the emission of visible light photons by a scintillation material when irradiated with ions. As the currently used material, known as TG-Green, is not commercially available anymore, a search of scintillation materials is made. The Tandem accelerator at 'Centro Nacional de Aceleradores' (CNA) is used to characterize the scintillation materials when irradiated with ions. Furthermore, a deposition technique is developed in order to create scintillator screens for their characterization, and for their use in different ion diagnostics. The present work proves the sedimentation technique is appropriate for the deposition of scintillators for ion diagnostics in fusion devices. Even though the literature showed other scintillators as optimal candidates, the experimental results have shown that, in terms of efficiency, the material TG-Green presents the highest absolute values compared with the analyzed materials.

Contents

Chapter 1

Introduction to nuclear fusion

1.1 World energy problem

The global CO_2 emission has reached 36.6 billion tonnes in 2018, while 87% of the greenhouse gas emissions comes from the production of energy [1]. The concentration of greenhouse gases accumulates as long as we are emitting. Thus, to cope with climate change, the CO_2 concentration in the atmosphere needs to stabilize. To achieve this, the world greenhouse gas emissions have to be reduced to net- zero following the Paris Agreement, which has as main goal is to keep the global warming below 2ºC before mid-century [2]. Living conditions are better where the gross domestic product (GDP) per capita is higher. Figure 1.1 shows the per capita CO_2 emissions against the GDP of each country in 2017. In every country where people's average income is above $25,000 per year the average emissions per capita are higher than the global average [1, 3]. Energy is essential to modern lifestyle and to any prosperous economy, but as fossil fuels are the dominant source of energy the access to modern energy implies that carbon emissions are too high. On the other side, those countries with a GDP per capita of less than $25,000 (left side of figure 1.1) have low carbon emissions. They lack access to energy. Since access to modern energy sources and technology is strictly related with living conditions, those that do not have sufficient access suffer poor living conditions. One of the problems of the developing countries is energy poverty [1].

Nowadays, approximately one-fifth of the world population, 1.4 billion people, live without access to electricity [5]. Population is expected to grow from 7.8 billion people in 2021 to 10.9 billions by 2100, so total energy demand will rise as well [2, 6].
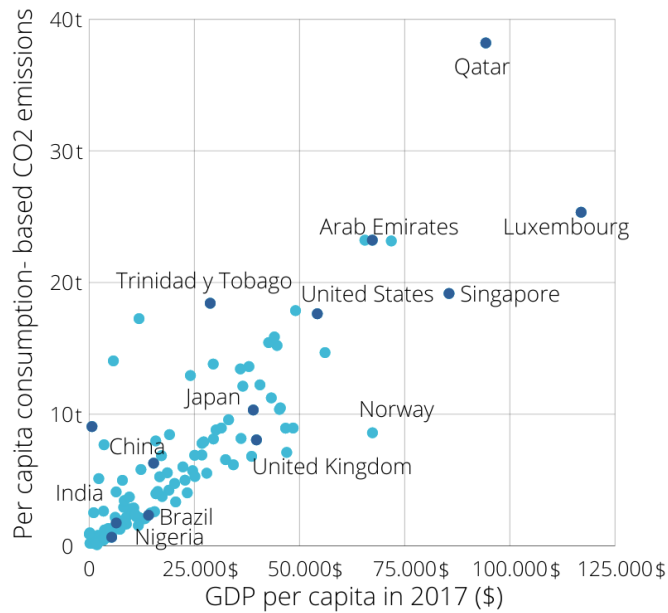
Figure 1.1: Consumption-based CO_2 emissions per capita vs GDP per capita in 2017. Data extracted from [1] and [4].

Finding a beneficial solution to the interrelated problems of population growth, energy poverty, energy scarcity, and global warming is one of the greatest challenges of the 21 st century.

1.1.1 Current low-carbon alternatives

Reducing the use of fossil fuels is key to solving some of the most important challenges of this century. Fossil fuels are coal, oil and gas. Combined, they are the largest source of global emissions of carbon dioxide. In contrast, the currently low-carbon sources are nuclear fission energy and renewable energy sources like hydropower, wind, solar, bioenergy and geothermal energy, amongst others.

Despite the fact that renewable energy is a low-carbon producer it has a number of disadvantages. The solar and the wind energy have an intermittent nature that is technologically uncontrollable [7]. Furthermore, they would require great amounts of land and new transmission lines that endangers the preservation of wildlife. Nuclear fission is a potential low-carbon source, but has the disadvantage of the transport and storage of radioactive waste [8].

As shown in figure 1.2, the energy sources currently used in the world are still dominated by fossil fuels. They account for more than 80% of energy consumption, while only the
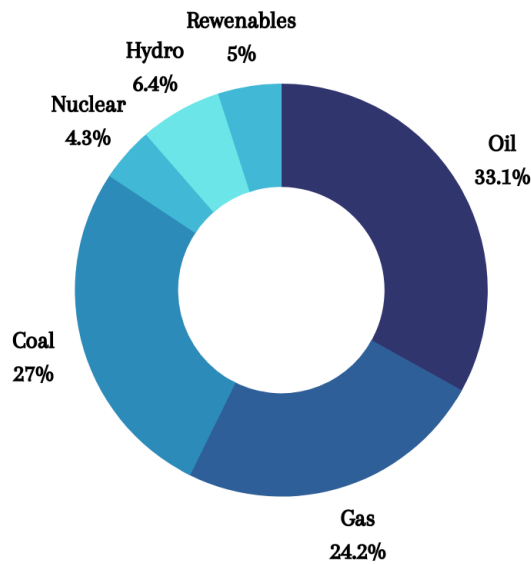
Figure 1.2: Global consumption of primary energy by fuel in 2019. Data extracted from [4] and [9].

15.7% of global primary energy comes from low-carbon sources, 11.4% from renewable energy and 4.3% from nuclear (2019). Hydropower and nuclear account for most of our low-carbon energy: combined they account for 10.7%. Wind produces just 2.2%, and solar 1.1% [4, 9]. The world needs to transfer from fossil fuels to an energy mix dominated by low-carbon sources of energy , but by 1994 we were already getting 13.5% from low-carbon sources, only two percentage points under the current number [1]. To achieve the necessary progress for the climate change we need to start replacing existing fossil fuels at a much faster rate; to fulfill the Paris Agreement, low-carbon alternatives must comprise 87-94% of global energy consumption by 2100 [2].

Currently, even though a low decarbonization is occurring, no low-carbon energy source is completely replacing the high amount of energy globally produced by fossil fuels [1].

1.1.2 Fusion energy

Fusion power would become a competitive large-scale electricity resource based on the fusion reaction (see section 1.2.1). It might be commercially available in the second half of this century [10]. Its exceptional characteristics might convert the fusion energy into a revolutionary low-carbon energy source that would contribute to solving the world energy problem. Fusion energy is:

Virtually unlimited: the fuels used in nuclear fusion are deuterium and tritium, both isotopes of hydrogen. While deuterium can be extracted from seawater, tritium can be obtained from lithium, which is also abundant in nature [11]. The primary fusion fuel is uniformly geographically distributed [10]. The abundant and cheap primary fusion fuel makes the fusion power a virtually unlimited energy source.

Sustainable: the pollution of the atmosphere does not occur during the normal operation of the reactor, as the products of the reaction do not contribute to the greenhouse effect [8, 10]. Tritium and the neutron activation of materials would be the only source of potential radiological hazards. Nevertheless, the half life time of tritium is only 12.3 years while the neutron activation is not as dangerous as the uranium in the case of nuclear fission. The product of the fusion process, besides a neutron, is helium, which is benign and can even be commercialized [12].

Secure: as fusion reaction is not a chain reaction and its control cannot be lost. Reactivity losses of the plasma in the event of an accident are limited by inherent processes, as plasma instabilities, within seconds [8]. Fusion reactors are under vacuum. In the case of an accident, the vacuum is lost and plasma discharge stops. As the fusion process will not generate long-lived radioactive waste, no transport of radioactive waste outside the plant is required [12].

1.2   Fusion basics

1.2.1   Fusion reaction

Fusion power is based on fusion reactions. Fusion reactions [13] occur when two or more nuclei combine to form another nucleus. For a fusion reaction to occur the nuclear force pulling the nuclei together must exceed the electrostatic force, i.e., the Coulomb interaction pushing them apart. Even if the kinetic energy of the reactant nuclei is lower than the Coulomb potential, the Coulomb barrier could be crossed due to the tunneling effect. Thus, the tunnelling effect reduces the energy (temperature) required for a fusion reaction to take place.

The amount of energy required to separate a nuclide into its constituent nucleons is called the difference in mass Δm, which is released in energy in accordance with $E = \Delta mc^2$. This energy is called the binding energy of the nucleus. It is represented in figure 1.3 against
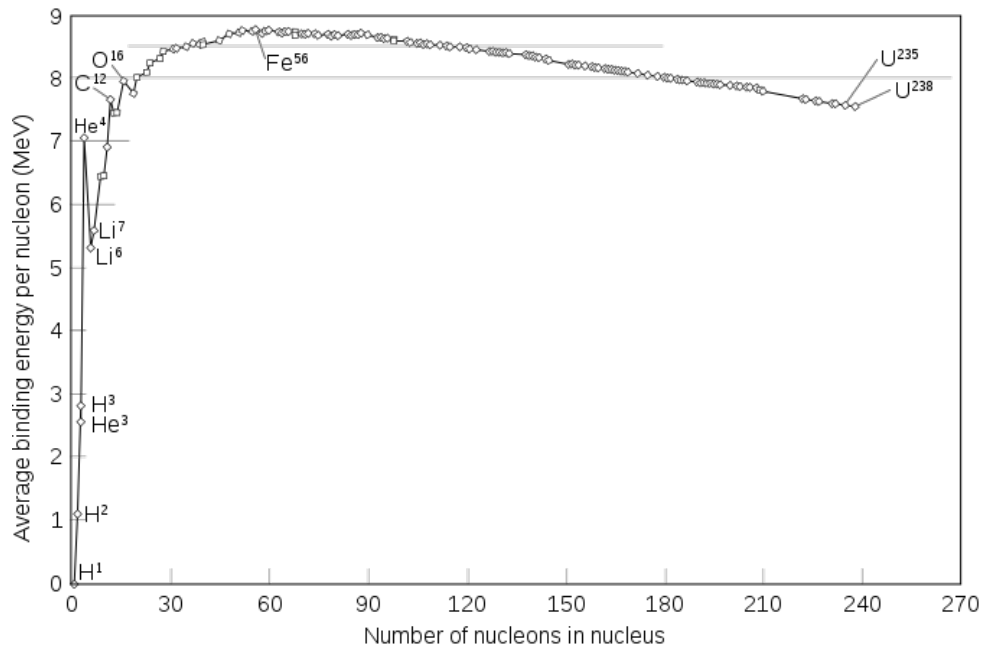
Figure 1.3: Average binding energy per nucleon against number of nucleons in nucleus. Extracted from [13].

the number of nucleons in the nucleus. The higher the absolute value of the binding energy the more stable the nucleus is.

In a nuclear reaction, if the mass of the initial nuclei is greater than that of the final nuclei, their difference will be positive and the energy will be released in form of kinetic energy of the nuclei formed in the reaction. Otherwise, it will be necessary to provide energy (generally in form of kinetic energy of the initial nuclei) for the reaction to occur. For nuclei lighter than iron-56 (figure 1.3), fusion reactions are exothermic, releasing energy. Different fusion reactions may be used to obtain energy in fusion reactors, being the most promising ones [14]:

$$D + T \rightarrow \alpha \ (3.5 \ \text{MeV}) + n \ (14.1 \ \text{MeV}) \tag{1.1}$$

$$D + D \rightarrow T \ (1.01 \ \text{MeV}) + p \ (3.02 \ \text{MeV}) \tag{1.2}$$

$$D + D \rightarrow {}^3He \ (0.82 \ \text{MeV}) + n \ (2.45 \ \text{MeV}) \tag{1.3}$$

$$D + {}^3He \rightarrow \alpha \ (3.6 \ \text{MeV}) + p \ (14.1 \ \text{MeV}) \tag{1.4}$$
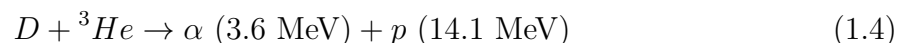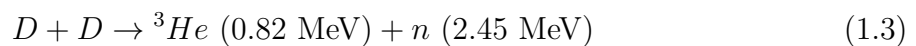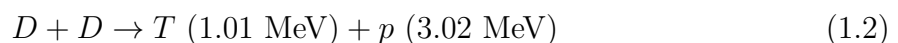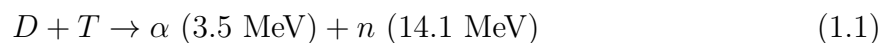
Here, D is deuterium, and T is tritium, two isotopes of hydrogen. The D+D reaction has two possible channels with approximately equal probability of occurring. The energy in the brackets is the energy released by them. The order of magnitude of the released energy (MeV) is many times greater than in a typical chemical reaction, which is of the order of a few KeV.
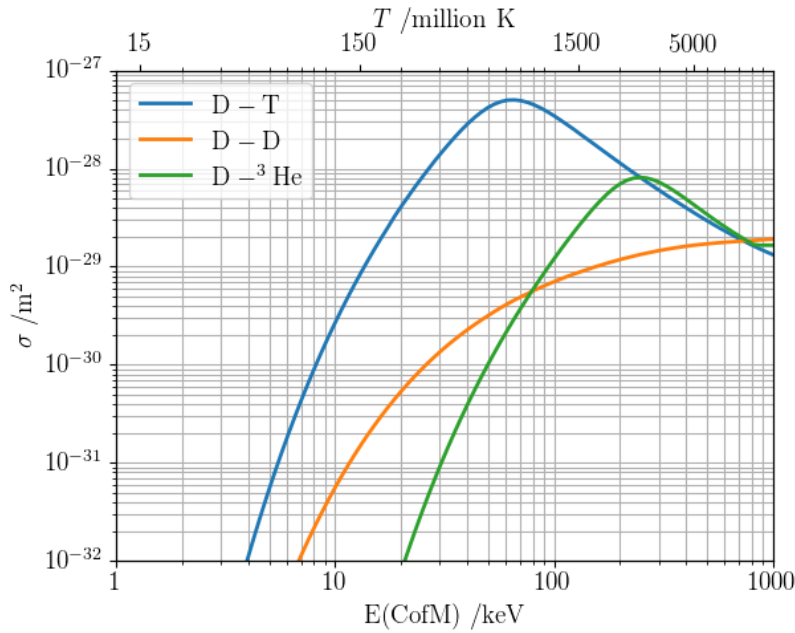
Figure 1.4: Fusion reaction cross section varying with the energy in a frame moving with the centre-of-mass (CofM) of the system. Extracted from [11].

Cross-sections for the fusion reactions outlined in equation (1.1)-(1.4) are shown in figure 1.4. The orange line depicts the total cross section for both processes involving D+D reaction. The D + T process has the largest cross section, which peaks at the lowest temperature. The cross-sections achieve their maximum in the range between 60-70 keV [14]. For this energy range the equivalent temperature order in Kelvin is given by the relation $E=k_B T$, where k_B is the Boltzmann constant, and it stays on the order of billion K [15].

This means that the plasma in which fusion occurs does not have to be heated as much: indeed, ITER aims to operate at 150 million K [16]. Nevertheless, even though ITER will employ the D-T reaction, the majority of the research on experimental fusion reactors has focused on the the D-D reaction, for example, in the case of ASDEX Upgrade (AUG) [17]. The D-D reaction is commonly employ in research due to it does not require an input of tritium or lithium, and the optimum energy to initiate this reaction is 15 keV [16], slightly higher than that for the D-T reaction.

Fusion reactions can be used to generate power through two different confinement systems, inertial and magnetic confinement. Inertial confinement initiates nuclear fusion reactions by compressing and heating targets filled with nuclear fuel, i.e., deuterium and/or tritium. The most extended method for inertial confinement employs lasers, but also high-energy beams of photons, electrons or ions can be used. Nevertheless, present work is focused on

magnetic confinement, which uses magnetic fields to confine fusion fuel in the form of a plasma.

1.2.2 Definition of plasma

As mentioned in section 1.2.1, for a fusion reaction to occur is necessary to supply energy by heating the fuel up to approximately 100 million K, depending on the reaction [16]. When high enough temperatures are reached, the fuel enters in a plasma state [17], which is defined as an ionized gas, *globally neutral*, that displays *collective effects*. Thus, it is formed by ions, electrons and a small fraction of neutral particles [16].

However, as the plasmas are formed mainly by charged particles, they have a characteristic behaviour. A fundamental parameter that defines the plasmas is the Debye length [13, 17]. If an electrically charged particle is introduced in a neutral plasma it would attract particles of the opposite charge that would surround the first one. The particles would produce a shielding effect on the particle that reduces its Coulomb potential. The resulting potential decreases exponentially with the distance. Consequently, the Debye length is defined as the distance in which the deviation from the Coulomb potential becomes significant. For a distance greater than the Debye length the plasma produces a *collective effect* as the introduced particle is not noticed, it is shielded. Thus, the *quasi-neutrality* condition [17] is complied when the dimension L of a system is much larger than the Debye length λ_D, which is expressed as [16]:

$$\lambda_D = \sqrt{\frac{\epsilon_0 k_B T_e}{n_e e^2}} \tag{1.5}$$

where ϵ_0 is the vacuum permittivity, k_B is the Boltzmann, T_e and n_e are the electron temperature and density, and e is the electron charge. Note that this expression depends only on electrons parameters as ions are considered static [13]. For example, for an electron density of $n_e = 5 \cdot 10^{19}$ particles/m^3 and an energy of $k_B T_e = 500$ eV the Debye length value is $\lambda_D = 1.42 \cdot 10^{-9}$ m.

1.2.3 Single particle motion

In this section, it will be explained how the particles that form the plasma move when they are under magnetic confinement. To this purpose, it will be focused on the single particle motion in an electromagnetic field [17].

A charged particle that is moving in an electromagnetic field will follow the Lorentz law.

The equation of the motion is:

$$\vec{F} = q\,(\vec{v} \times \vec{B} + \vec{E})$$

(1.6)

where q and $\vec{v}$ refer to the charge and velocity of the particle and $\vec{B}$ and $\vec{E}$ stand for the magnetic and electric fields. Under the assumption of uniform electric and magnetic fields, the movement of the charged particle describes circular paths that orbit a guiding center. The movement is then helical around the magnetic field lines. The velocity component in the plane perpendicular to the magnetic field is called the perpendicular velocity, $v_\perp$, while the parallel velocity, $v_\parallel$, is the velocity component along the magnetic field lines. The parallel velocity is unrelated to the transverse components and can be treated separately.

The frequency of the circular motion is called gyrotron frequency, w_c, and is described by equation (1.9):

$$w_c = \frac{|q|B}{m}$$

(1.7)

where m is the mass of the particle, The radius of the circular path is called Larmor radius:

$$r_L = \frac{mv_\perp}{|q|B}$$

(1.8)

and it depends on the mass of the particle m, its charge q, the perpendicular velocity $v_\perp$, and on the magnetic field $\vec{B}$. The pitch angle is the angle between the ion velocity and the magnetic field line, this is:

$$\lambda = \frac{v_\parallel}{v}$$

(1.9)

An electric field in the plasma causes the drift of the guiding center, $\vec{v_E}$, in the perpendicular direction to the magnetic field:

$$\vec{v_E} = \frac{\vec{E} \times \vec{B}}{B^2}$$

(1.10)

This expression is independent of the perpendicular velocity. In the first half-cycle of the orbit of the ion, it gains energy from the electric field and increases in $v_\perp$, hence, in r_L. In the second half-cycle, it loses energy and decreases in r_L. This difference in r_L on the left and right sides of the orbit causes the drift of the guiding center. The motion is the sum of the circular Larmor gyration plus the drift of the guiding center. The three-dimensional orbit in space is therefore a helix with changing pitch.
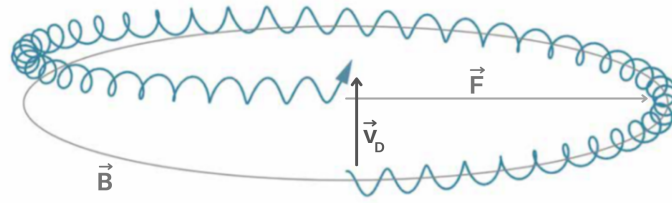
Figure 1.5: Helix motion of a positively charged particle with the drift of the guiding center. Extracted from [13].

Generally, when there is a force on the particles perpendicular to the magnetic field, then they drift in a direction perpendicular to both the force and the field. If $\vec{F}$ is the force on one particle, then the drift velocity is:

$$\vec{v_D} = \frac{\vec{F} \times \vec{B}}{qB^2} \tag{1.11}$$

When a non-uniform $\vec{B}$ field is applied, the gradient in $|\vec{B}|$ causes the Larmor radius to be larger where the magnetic field is larger. This fact leads to a drift that is perpendicular to both $\vec{B}$ and $\nabla\vec{B}$ and it is in opposite directions for ions and electrons. This charge separation causes a current transverse to $\vec{B}$. The mentioned drift is called the $\nabla-$B drift, $v_{\nabla B}$, and its expression is:

$$\vec{v_{\nabla B}} = \pm\frac{1}{2}v_\perp r_L \frac{\vec{B} \times \nabla\vec{B}}{B^2} \tag{1.12}$$

When the lines of force are curved with a radius of curvature, R_c, the average centrifugal force depends on the component of velocity along $\vec{B}$, $v_\parallel$. This force gives rise to a drift called the curvature drift, v_R:

$$\vec{v_R} = \frac{mv_\parallel^2}{qB^2} \frac{\vec{R_c} \times \vec{B}}{R_c^2} \tag{1.13}$$

In practice the $\nabla-$B drift will always be added to the effect of the curvature drift, so no cancellation is possible.

The charged particles that form the plasma will be confined by magnetic fields, thus, they will follow the Lorenz law and suffer from drifts in a fusion device called Tokamak.

1.3   The tokamak reactor

A tokamak [16] is a toroidal magnetic plasma confinement system, which is projected as a future fusion reactor. In a tokamak, the plasma is confined by a magnetic field. In magnetic confinement fusion [14] the electromagnetic properties of the charged plasma particles are used to trap them away from the walls of the reactor. Plasma confinement is achieved by combining magnetic fields produced by different sources. The main magnetic field is the toroidal field. A series of nested ring coils (see figure 1.6) induce a magnetic field with a toroidal shape. However, a purely toroidal magnetic field cannot confine the plasma particles. Due to the toroidal shape of the field, the particles suffer curvature and $\nabla-B$ drifts, leading to a charge separation. The consequent electric field gives rise to fast losses of the plasma particles towards the walls. To prevent the charge separation, it is important to twist the magnetic field lines. To this aim, a poloidal magnetic field is introduced by a plasma current [13] that flows in the toroidal direction. This current is produced by a central solenoid which is formed by the inner poloidal field coils in figure 1.6. Through an increasing electric current in the solenoid, these coils induce the current in the plasma. In this way, this solenoid behaves like the primary transformer, while the plasma current acts as the secondary transformer (see figure 1.6).

on the minor cross-section of the torus. A central solenoid, behaving like the primary from a transformer, induces a current over the plasma. It is formed by the inner poloidal field coils in figure 1.6. Through an increasing electric current, these coils induce another current in the plasma itself, as it is made of charged particles. The plasma current [13] flows in the toroidal direction, acting as the secondary transformer circuit. The main disadvantage of the way in which the poloidal field is generated in a tokamak is that the magnitude of the primary current must increase continuously to maintain the induction. The impossibility of increasing this current without limit leads to a pulsed operation. Additional, poloidal field coils are used to position and shape the plasma (see figure 1.6). The combination of the toroidal and poloidal fields gives rise to helical magnetic field lines that turn around the torus, as shown in figure 1.6.

1.3.1   External plasma heating

The initial heating in tokamaks comes from the ohmic heating [16] caused by the toroidal current. The energy obtained by ohmic heating decreases with the temperature. Consequently, the ohmic heating itself cannot drive the plasma to the required temperature for
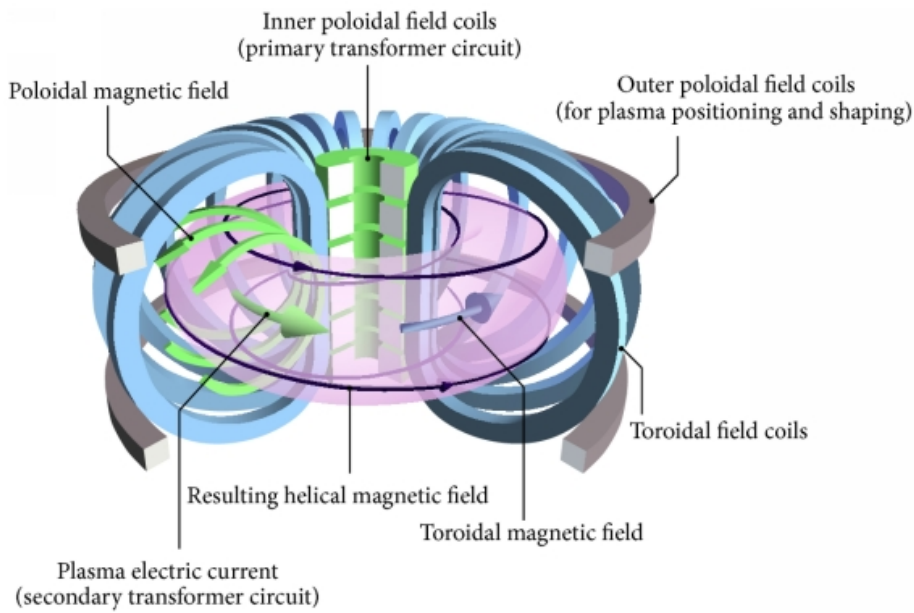
Figure 1.6: The magnetic system of a tokamak. Extracted from [18].

a fusion reaction to occur, leading to the requirement of additional heating. As illustrated in figure 1.8, fusion devices are equipped with external heating systems to lead the plasma to the desired temperature.

Neutral Beam Injector (NBI) [15, 16]. High energy neutral particles (normally deuterium or hydrogen from 60 to 100 keV in AUG), are injected into the plasma so they can interact with plasma particles. High energies are used so that the neutral particles can penetrate deep into the plasma core. To generate the neutral particles, the NBI system uses an ion source. The beam ions are accelerated within a high voltage grid and are then neutralized in a gas cloud. Once the neutrals are injected into the plasma, they interact with plasma particles by three different mechanisms: by charge-exchange reactions with plasma ions, by ionization due to collisions with electrons, or by ionization due to collisions with ions. As shown in figure 1.8, the charge exchange cross section dominates at energies lower than 50 keV per atom while ionization by ion collision dominates at higher energies.

Radio frequency heating (RF) [14]. This system is based on launching electromagnetic waves in the plasma using an antenna so that the waves interact with the plasma particles. To this aim, resonance between the electromagnetic wave and an ion or an electron is necessary, being the wave frequency a multiple of the particle cyclotron frequency, w_c. There are two different types of radio frequency heating: resonance with electrons by Electron Cyclotron Resonance Heating (ECRH), and resonance with ions by Ion Cy-
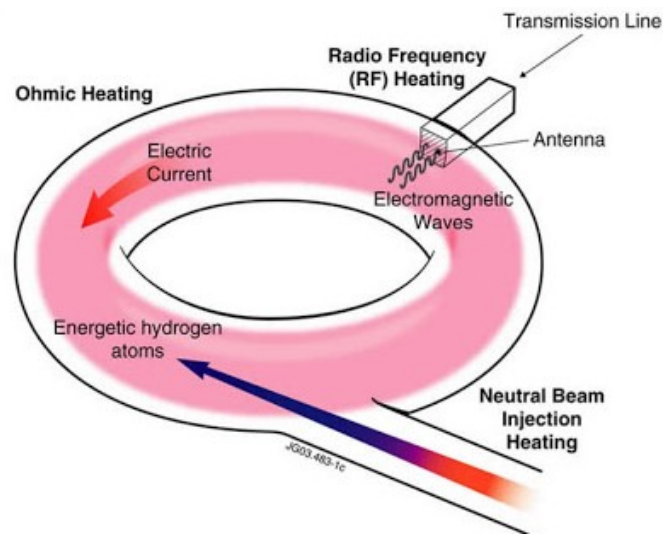
Figure 1.7: External plasma heating systems. Extracted from [19].
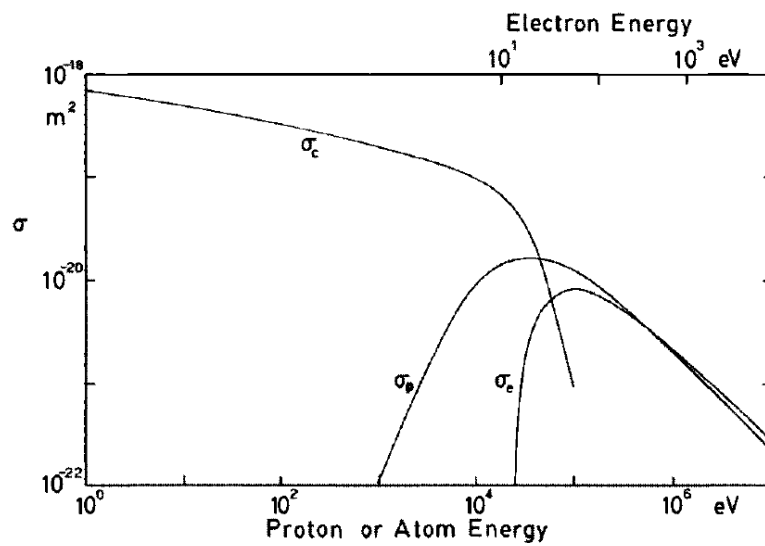

Figure 1.8: Mechanisms by which a neutral particle can become an ion inside a plasma. Charge exchange (σ_c), collision with electron (σ_e) and collision with proton (σ_p). Extracted from [20].

clotron Resonance Heating (ICRH). Normally, ICRH is used with a frequency from 30 to 80 MHz. As the resonance condition will be satisfied at a localised position, usually near the center of the plasma, the antenna is adjusted so it creates a significant population of 'hot' particles in the plasma core.

1.3.2 Fast-ion population

Common to the heating systems previously presented is that the energy is transferred to the plasma by a population of high-energy ions. Their speed is highly above that of the thermal particles in the bulk of the plasma. The fast-ion population [21] stores a fairly large fraction of the energy in the entire plasma. For this reason, the behaviour of the fast-ions is of importance for the overall plasma dynamics. In future reactors, the main source of supra-thermal particles will be the energetic alpha particles created in fusion reactions, while in present-day tokamaks they are created mostly by NBI and ICRH. The confined fast-ion population outlines the heating profile, so it affects the transport, the temperature and the density profiles of the plasma. The coupling between the fast ion-population and the bulk plasma affects the plasma stability, being of significance both the spatial and the velocity distribution of the fast-ion population. Several processes could affect the fast-ion population, leading to fast-ion losses [22] that concern the heating efficiency and the damage of the reactor vessel. Magnetohydrodynamics fluctuations (MHD) or prompt losses (particles which are directly injected in non-confined orbits) are examples of events that could lead to fast-ion losses.

1.4 Scintillator-based plasma diagnostics

Fast-ion confinement is essential to produce stable and efficient plasmas in current and future tokamaks. Therefore, understanding the mechanisms that lead to the loss of these highly energetic particles is mandatory. To this end, scintillator-based diagnostics have proved as a fast and highly efficient [23] way of studying the phenomena that produce the fast-ion losses. The Plasma Science and Fusion Technology group (PSFT) of the University of Seville has lead and participated in the design, construction and operation of several scintillator-based diagnostics in fusion reactors world-wide such as ASDEX Upgrade (Germany) [24], TCV (Switzerland) [25], JT60-SA (Japan) [26] or DIII-D (USA) [27].
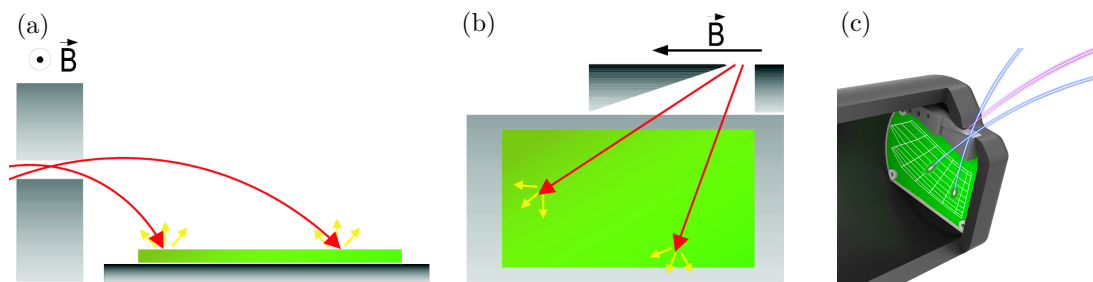
Figure 1.9: Overview of the FILD diagnostic: (a)Top view (b)Lateral view (C)3D view. Extracted from [28].

1.4.1   Fast-Ion Loss Detectors

The Fast-Ion Loss Detector (FILD) [22] resolves the velocity space of the fast ions with fast ($\sim$100 kHz) temporal response. The detector enables the evaluation of the effect of the perturbations that affect the fast-ion population (see section 1.3.2) by measuring the gyroradius (energy), the pitch angle and the flux of the fast-ion losses.

The FILD diagnostic works as follows: the local magnetic field disperses the ions onto a scintillator material (see figure 1.9). The fast-ions enter the FILD diagnostic through a pinhole, pass through a collimator and strike the scintillator plate. A light pattern is then generated and imaged by a camera and a photomultiplier (PMT) array. The strike points depend on the gyroradius of the particle (its energy) and the pitch angle. The camera provides a high spatial (energy-pitch angle) resolution, while the array of PMTs enables a time resolved measurement of 1 MHz bandwidth.

1.4.2   Imaging Neutral Particle Analyser

The interplay between fast-ions and the plasma particles could occur through the mechanism of charge exchange reactions (CX) [28] (see section 1.3.1). In these reactions an electron is transferred from the neutral plasma particle to the fast-ion. The new neutral maintains the energy and momentum of the initial ion. The fast neutral particle can escape the plasma as it is not confined by the magnetic field. The Imaging Neutral Particle Analyser (INPA) [20] measures the velocity of the escaping neutrals and, therefore, the velocity of the 'old' confined fast-ion. To this end, when the fast neutrals reach the detector, they are ionised by an ultra-thin carbon foil and are then deflected onto a scintillator (see figure 1.10). The strike position of the particles in the scintillator will be given by their energy and velocity orientation (pitch angle). Thanks to the use of an NBI as neu-
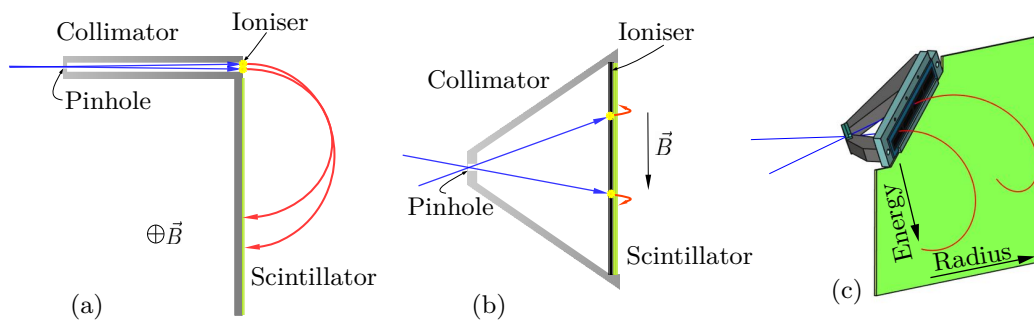
Figure 1.10: Scintillator plate in AUG INPA: (a)Lateral view (b)Top view (c)3D view. Extracted from [28].

tral source, a one-to-one relation can be established between the velocity orientation of the neutral and the radial position of the confined fast-ion. The light pattern is collected by a series of lenses and guided to a camera that provides high resolution images of the scintillator, and a series of PMT which allows for fast time resolved measurements (up to 100 kHz are expected for the AUG INPA diagnostic [20]).

1.4.3 Imaging Heavy Ion Beam Probe

The Imaging Heavy Ion Beam Probe (i-HBIP) [29, 30] is a diagnostic that allows the characterization of small and large scale fluctuations, by providing measurements of density, potential and poloidal magnetic field perturbations at the edge of the plasma. The diagnostic (see figure 1.11a) uses a neutral primary beam to inject heavy ions into the plasma. In the case of the i-HIBP diagnostic installed in ASDEX, the beam consists of cesium or rubidium atoms with an energy up to 100 keV. The neutral atoms are ionized by collisions (see figure 1.11a) with the plasma particles and introduce a fan of secondary ions that is deflected by the Lorentz force and then collected by a scintillator. This produces a light pattern that is detected by a fast camera and has the shape of a line. The intensity of the light pattern is determined by the plasma density while its location and shape is determined by the magnetic field and the electrostatic potential. As shown in figure 1.11b, the magnetic field perturbations lead to an offset of the whole light pattern, whereas an electrostatic potential perturbation deflects the light pattern only locally. This way magnetic perturbations can be discriminated from electrostatic potential perturbations.

(a) i-HIBP working principle

(b) Light pattern seen by the camera
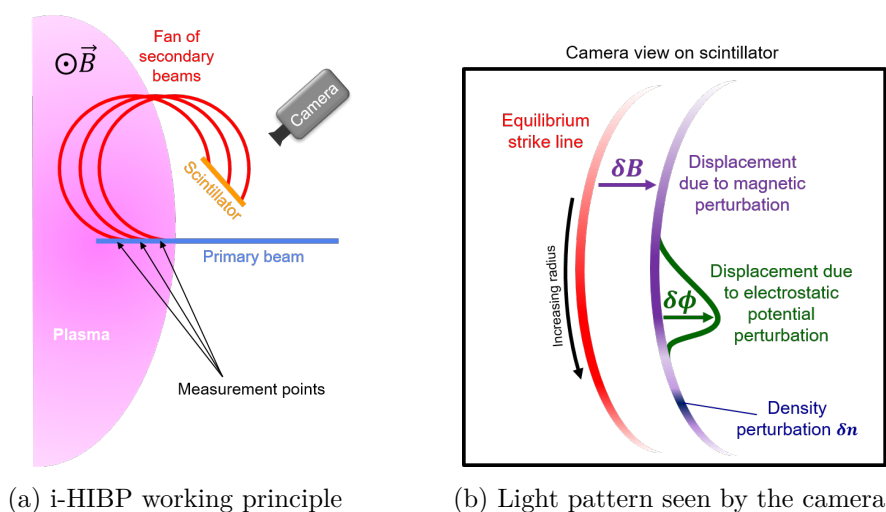
Figure 1.11: Scintillator plate in i-HIBP diagnostic. Extracted from [30].

1.5 Objectives of this master thesis

To ensure a good output signal in the previous exposed diagnostics, the scintillation material becomes a decisive component. In this master thesis the main objective is the search of different commercial scintillation materials, and their characterization for the specific conditions that the diagnostics in section 1.4 require. Furthermore, the process that transforms the scintillation materials from powders to a deposited screen on a plate, the deposition technique, will be treated with a double purpose: the coating of the scintillator plates needed for the diagnostics, and the deposition of different materials to analyse them and identify which one is the most adequate for ion diagnostic application.

Chapter 2

Scintillation materials

The ion detection diagnostics described in section 1.4 need a scintillator material with high efficiency that allows a good signal level and a fast decay time to follow the plasma fluctuations [23]. In this chapter, a brief description of the key concepts that involve the scintillation process is included, followed by the description of the light emission mechanism of the scintillator materials. After that, the main conditions that a scintillator material might comply for ion diagnostic application will be discussed, and the search of materials that are nowadays commercially available is shown. Finally, the consequent selection of materials that could be optimum for their application in nuclear fusion reactors is exposed.

2.1 Scintillation basics

2.1.1 Key concepts

The general term that describes the phenomenon of light emission (output) by a material as a result of any excitation source (input) is called luminescence [31]. 'Luminescence' encompasses many different processes, depending on the excitation source [32, 33] (see figure 2.1). For example, when the excitation of the material originates from a chemical reaction, the process is called 'chemiluminescence'. When the excitation source is specifically induced by ionizing radiation the process is called scintillation [34]. However, the light emission of the scintillation process depends on the type of incoming particle. In the case of the diagnostics described in section 1.4 the excitation is caused by different ions, and thus, the scintillation process is called 'ionoluminescence' in the case under study.
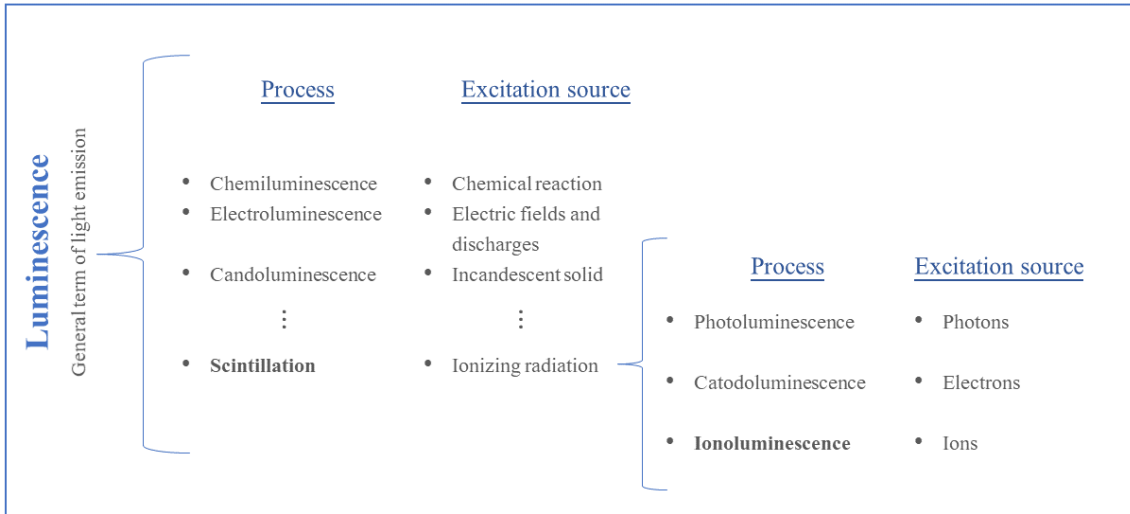
Figure 2.1: Luminescence processes.

The luminescence materials could be either organic or inorganic. Inorganic scintillators have the highest output of light intensity, i.e., they deliver a larger amount of photons per unit of absorbed energy. This fact translates into a better resolution in energy of the ionizing particle, the input, to be measured [31]. As a consequence, only inorganic materials will be taken into account for the present work (see section 2.2.1).

'Fluorescence' is an instantaneous process, referring to the time scale of atomic transitions. This phenomenon occurs when the emission of light is on the order of 10 ns after the interaction of the radiation with the material. Organic scintillators usually have decay time of this order, thus they are also called *fluorescent*. If the emission is delayed to the process it is called 'phosphorescence'. In general, inorganic scintillators have a decay time of the order of 300 ns, hence they are commonly named *phosphors* [35], even though they are not necessarily composed of phosphor. This nomenclature is is used in the following.

2.1.2   Mechanisms of light emission

Inorganic scintillators are crystal materials with an ordered internal structure. Their regular crystalline lattice is the basis for the scintillation process. In these structures the electrons have available only discrete bands of energy [36]. The lower band, called valence band, represents those electrons that are essentially bound at lattice sites, whereas

the conduction band represents those electrons that have sufficient energy to be free to migrate throughout the crystal. There exists an intermediate band of energies, called the forbidden band, in which electrons can never be found in the pure crystal [37].

When high-energy particles reach the materials, they will suffer a Coulomb interaction with the electrons of the valence band, that will move at different levels in the conduction band [34]. The electron leaves a hole in the valence band and occupies a position in the conduction band. An electron-hole pair is created.

Small amounts of an impurity are commonly added to inorganic scintillators, creating special sites in the lattice at which the energy band structure is modified from that of the pure crystal. These sites reduce the de-excitation energy and are called luminescent centers. The light emission occurs due to the relaxation of excited luminescent centers by emitting a photon. As the energy of the luminescent centers is lower than the gap energy, the emitted photons belong to the visible light. As a consequence, the energy structure of the impurity (or dopant) determines the emission spectrum of the scintillator [38]. Furthermore, all the excited configurations of the dopant are formed essentially at once and will subsequently de-excite with the half-life characteristic of the excited state. It is the characteristic time of these states that therefore determines the decay time of the emitted scintillation light, which are of the order of 30-500 ns [36]. There are other processes that compete with the one just described giving rise to a slow component that can often be a significant source of background light or 'afterglow' in scintillation.

2.2   Selection of plasma diagnostic scintillators

2.2.1   Requirements of the ion diagnostics

There are several aspects that the scintillation material must comply when used in plasma diagnosis. In the harsh environments encountered in fusion devices, the scintillator material must have [23, 36, 39]:

- *High light yield*: when irradiated with particles involved in the diagnostics described in section 1.4, that is [20, 30]:

    - Fusion born α-particles, with an energy of 3.5 MeV (FILD).

    - Deuterium ions originated from neutral beam injection (NBI) with an energy from 0.1 to 1.0 MeV (FILD and INPA).

– Ion Cyclotron Resonance Heating (ICRH) origin protons, deuterium, tritium and α-particles from 0.1 to 10 MeV (FILD).

– ^{133}Cs or $^{85/87}Rb$ atoms used as primary beam injection (i-HIBP).

- *Fast decay time*: fast response in the nanosecond range in order to identify the MHD fluctuations responsible for the fast-ion losses in a range up to 1 MHz.

- *Emission peak in the visible range (380-750nm)*: the wavelength range should preferrably be in the range of visible light to be measured by cameras and photo-multiplier tubes. The specific range in which the quantum efficiency (QE) of the electronics (cameras and PMTs) is high, preferrably more than 50%, varies depending on the models employed in each diagnostic. At AUG FILD, for example, a CCD camera with 50% of QE in the range 450-800 nm, is used.

- *Resistance to temperature* [40]: as the light yield and decay time depends strongly on the operation temperature, scintillation materials should emit light when irradiated with the ions of interest in the temperature range between 400 to 700K.

- *Linearity*: the conversion of the ion energy into detectable light should be linear, i.e., the light yield should be proportional to deposited energy over a range as wide as possible.

- *Low sensitivity to other radiation sources*: such as neutrons, electrons, X-rays and γ-rays.

  As mentioned in section 1.5, and apart of the properties of the materials, the deposition of the powders giving place to a scintillator screen leads to several requirements that the screen must comply:

- *Thickness*: the stopping power of the scintillation materials when irradiated with the ions of interest imply different particle radiation lengths. The radiation length changes with the energy of the incoming particle. The thickness of the scintillation screen must be large enough to ensure that the energetic particles to be studied can deposit all their energy.

- *Resistance to vibrations*: in a tokamak, the scintillator screen is subjected to inner operation vibrations, so the scintillator screen must have a high enough adherence and robustness to avoid material leaks.

- *Ultra-high vacuum compatibility*: the scintillator screen will be placed in an ultra high vacuum chamber and thus, the material has to be compatible with it. The ultra-high vacuum regime is characterized by pressures in the range of 100 nPa.

2.2.2 Commercial scintillators

During the last years, the most widely used scintillation material employed in plasma diagnostics is *TG-Green*, chemical formula $SrGa_2S_4$:Eu. Numerous previous studies of ionoluminiscence [23, 39, 40, 41, 42] have shown its better efficiency, in comparison with other scintillators, and its fast response of 500 ns. To date, TG-Green is still the most adequate material for ion detection diagnostic in fusion devices. Nevertheless, it is not commercially available anymore, and only a few enterprises around the world still manufacture it. This fact leads to the research of new scintillation materials with the same or better properties than the well known TG-Green, but with commercial availability. In the present work, new materials are identified and tested in order to look for competitors that that may replace TG-Green.

The selection of new phosphors is made from a large catalogue of manufacturers, following these criteria:

- Commercial availability

- Decay time on the order of several ns

- Peak emission in the visible light range (380-750 nm)

As mentioned in section 2.1.1 regarding the efficiency of the materials, the data provided by manufacturers will not be used as a criterion. The selected materials are tested through ionoluminescence probes to ensure the efficiency specific to the ion diagnostic purpose, and are compared to the efficience of TG-Green. Taking into account the previous mentioned criteria, the following selection of scintillation materials was made (see also Table 2.1).

2.2.3 Selected materials

In the most important commercial applications of luminescence materials the excitation is not induced by ions. This fact hinders the search of appropriate materials by looking at the data available in bibliography, making it necessary to study the ionoluminescence

Name	Formula	$\lambda(nm)$	$\tau(ns)$	$\rho(\text{g/cm}^3)$	Manufacturer	Ref
Currently used compounds						
TG-Green	$SrGa_2S_4$:Eu	530	540	3.65	Yujii	[23] [39][40][41][42]
YAG	$Y_3Al_5O_{12}$:Ce	535	300	4.55	Yujii, PhosphorTech, Nemoto, Mitsubishi, Phsophor Technology	[32][34][36][39][41]
ZnS	ZnS:Ag	450	200	4.09	PhosphorTech	[39]
Yttrium compounds						
YAP	$YAlO_3$:Ce	370	27	5.37	Crytur, Advetch, Phosphor Technology	[32][34][36][43]
YAGG	$(Y, Ga)_3Al_5O_{12}$:Ce	550	550	5.28	Standford, Phosphortech, Phosphor Technology, Mitsubishi	[44]
YAGGd	$(Y, Gd)_3Al_5O_{12}$:Ce	570	106	4.69	Phosphortech	[44][45][46]
Lutetium compounds						
LuAG	$Lu_3Al_5O_{12}$:Ce	540	71	6.7	Yujii, Mitsubishi, Phosphortech, Baikowski, APN	[34][46]
LuAP	$LuAlO_3$:Ce	365	2500	8.54	Advetch	[34][36][43]
LuSiO	Lu_2SiO_5:Ce	420	40	7.4	Phosphor Technology	[34][36]
Silicates Compounds						
β-sialon	$Al_3N_4Si_3O_4$:Eu	530	912	4.01	Mitsubishi,Yujii	[47][48][49]
Others						
ZnO	ZnO:Ga	500	15	5.63	Phosphor Technology	[50][51]
CaWO	$CaWO_4$	430	8000	6.1	Phosphor Technology, APN, Sigma Aldrich	[34][36]
GOS	Gd_2O_2S:Tb	545	600	7.34	Phosphor Technology	[52]
LSN	$La_3Si_6N_{11}$:Ce	535	100	-	Mitsubishi	
LYSN	$(La, Y)_3Si_6N_{11}$:Ce	550	100	-	Mitsubishi	
CSO	$CaSc_2O_4$:Ce	516	100	-	Mitsubishi	

Table 2.1: Inorganic commercial scintillators properties. From left to right: commercial name, chemical formula, peak emission, characteristic decay time, density, manufactures and references.

to ensure the use of efficient materials. Nevertheless, there are some previous studies of ionoluminescence that guide the present work. Those are the basis for the final selection of materials that are characterized in this work.

- **YAGG and YAGGd**

  One of the main competitors of the TG-Green scintillator is the Yttrium Aluminium Garnet, YAG [53]. It is an efficient and fast material, with an extended use in different applications, and with a high commercial availability. However, its efficiency is not as high as the TG-Green efficiency when submitted to ionoluminescence [22, 39, 41, 42]. Other studies [39, 41] reveal that, even though most of scintillators belong to the yttrium family, common yttrium compounds are slower (with decay times in the milisecond order) in comparison with YAG, so they were discarded. However, two new materials that result as a modification of YAG, but with faster decay times, are studied here. These are YAGG and YAGGd [45, 46], which have a chemical formula that is similar to the classic YAG but incorporating galium and gadolinium, respectively. They have the better results in terms of γ-ray luminescence efficiency compared with YAG [44].

- **YAP**

  Previous studies demonstrate that the low-energy (<40 keV) ionoluminescence efficiency of Yttrium Aluminium Perovskite, YAP [32], is higher than that of the currently TG-Green phosphor and its decay time is optimum. Despite its good characteristics, its peak emission is close to the low limit of visible light. This fact is a disadvantage since it could be a problem for the electronic chain to measure a stable signal. Furthermore, its availability is not so frequent although some manufacturers offer it.

- **LuAG**

  Lutetium Aluminium Garnet, LuAG [46], has a good decay time of 100 ns and a peak emission (540 nm) similar to other scintillation materials used in fusion devices. It has never been used before for ion detection diagnostics, but may be a possible candidate with high availability.

- **β-sialon**

  The β-sialon [47, 48, 49] ionoluminescence spectra peaks at wavelengths of 540 nm, which lies in the preferred range of general optical sensors. Furthermore, as the
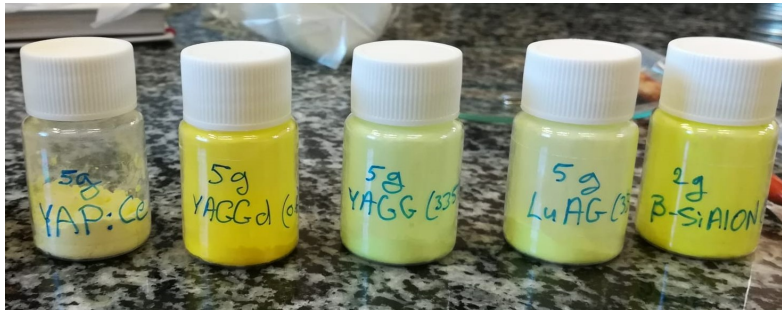
Figure 2.2: Materials under study. From left to right: YAP, YAGGd. YAGG, LuAG and β-sialon.

irradiation progresses, the phosphor remains largely unchanged. The thermal resistivity of this compound has been measured by ionoluminescence under temperature control. The ionoluminescence intensity retains half of its original value at the highest temperature of 773K. These experimental results reveal that β-sialon could be a potential candidate for a scintillation monitoring tool for harsh environments in which intense beam irradiation at high temperature can be expected.

Even though the fast decay time and visible light peak emission are two essential requirements in the selection of an appropriate scintillator, additional properties affect the final decision, as outlined in section 2.2.1. In the present work, the selected materials are subject to ionoluminiscence measurements in order to obtain their relative efficiencies in relation to the efficiency of TG-Green. To this end, the scintillators YAP, YAGGd, YAGG, LuAG and β-sialon have been bought (see figure 2.2). The treatment of the powders shown in figure 2.2 to obtain homogeneous scintillator screens is described in the following chapter.

Chapter 3

Deposition technique

Ionoluminescence measurements of the materials selected in chapter 2 are performed to obtain their relative efficiencies and compare them to the efficiency the efficiency of TG-Green. The deposition technique is the laboratory process by which the phosphor powders are transformed into a scintillator screen. The development and evolution of this technique is presented in the next chapter.

3.1 Deposition technique at CNA

3.1.1 Technical background

Previously, a deposition technique has been developed by the Plasma Science and Fusion Technology Group at CNA [39, 42] with the aim of manufacturing the scintillator screens ourselves. The phosphor deposition is done through a sedimentation process, which is the starting point in the present work. The materials needed are the following [42]:

Materials and reagents

- Beaker
- Petri dish with a lid
- Watch glass
- Pipette
- Balance
- Magnetic stirrer with heating

- Drying oven
- Scintillator powders
- Deflocculant: sodium docusate ($C_{20}H_{37}NaO_7S$)
- Distilled water

Experimental procedure

First, 10 ml of distilled water is poured into the beaker. After that, 1 g of scintillation phosphor is put on the watch glass and weighed in the balance. The powders are introduced into the beaker with a spatula. The beaker is put on the magnetic stirrer, which is configured such that the revolution in which the stir bar does not vibrate much, but at the same time it does not become slow, normally 200 rpm for a 25 ml stir bar. The mixture must be stirred 10 minutes. The phosphor tends to sediment the moment the stirrer stops.

While the phosphor in water is stirred, the adhesive is weighed. The needed adhesive quantity is 1% of the phosphor weight. The adhesive is added to the mixture and the heating temperature is fixed to 60ºC. The mixture is stirred and heated 10 more minutes. A diagnostic scintillator plate (commonly made of stainless steel) is put in a Petri dish. When the mixture is finished it is deposited onto the plate using a magnet bar to hold the stir bar. The screen is left to dry air during 24 hours with the lid on, so air contaminants do not reach the mixture. After that time, the phosphor is deposited on the plate. The excess of water is slowly extracted with the pipette. Finally, the deposited plate is put into the oven during 10 minutes at 140ºC.

Results

The final result is shown in figure 3.1a. This sedimentation technique achieves high-quality results, comparable with the scintillator plates deposited by manufacturers. Nevertheless, the plates are under harsh environments when used in ion diagnostic detectors at fusion devices (see section 2.2.1). Screens deposited by this method, but also deposited by manufacturers, present a sandy texture with low adherence between the scintillator and the plate. As an example, at figure 3.1b shows how some of the phosphor powders detached during the operation of the diagnostic. This can affect the signal of the diagnostics, and thus should be avoided. One of the main objectives of this work is to improve the robustness, adherence and homogeneity of the scintillator screens in order to improve their resistance during operation. To this end, several modifications of this technique are
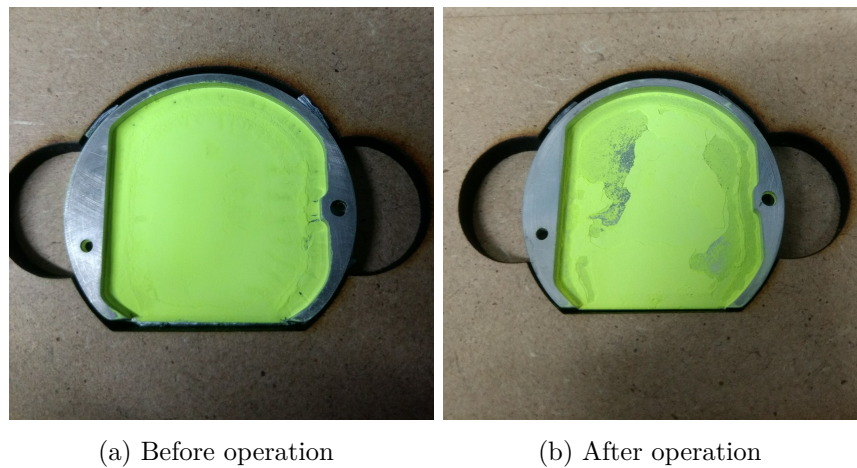
(a) Before operation   (b) After operation

Figure 3.1: Aspect of the scintillator sample before and after being used for a FILD diagnostic at DIII-D Tokamak.

made in section 3.1.3, while a theoretical background is introduced first.

3.1.2 Theoretical background

Colloidal dispersions

The mixture prepared with the phosphor and the distilled water is called a colloidal dispersion. The composition of a colloidal dispersion is solid, liquid or gas particles dispersed in a continuous phase (solid, liquid or gas). Normally, the term colloidal refers to particles with dimension ranging from 1nm to 1µm. In this case, as the phosphor powders are in solid state while the dispersant will be distilled water or ethanol, the colloidal dispersion is called *suspension*.

Suspensions are unstable. The physical stability of suspensions could be defined as a condition in which the particles do not aggregate and remain homogeneously distributed in the suspension over a certain time, without sediment or separate in phases (See figure 3.2). For the deposition process described in section 3.1.1, when the stirring of the phosphor suspension is stopped, the two phases (phosphor and water) are immediately separated. The stability of a colloidal system is inevitably linked to a notion of time, defined by the process. It is important for the sedimentation process that this time is high enough, so the particles sediment (fall to the bottom) slowly and one by one. In that way homogeneous screens are obtained. If all the particles suddenly fall at the same time, the screen is more probably to be irregular. The way in which the phosphor powders are mixed into the water
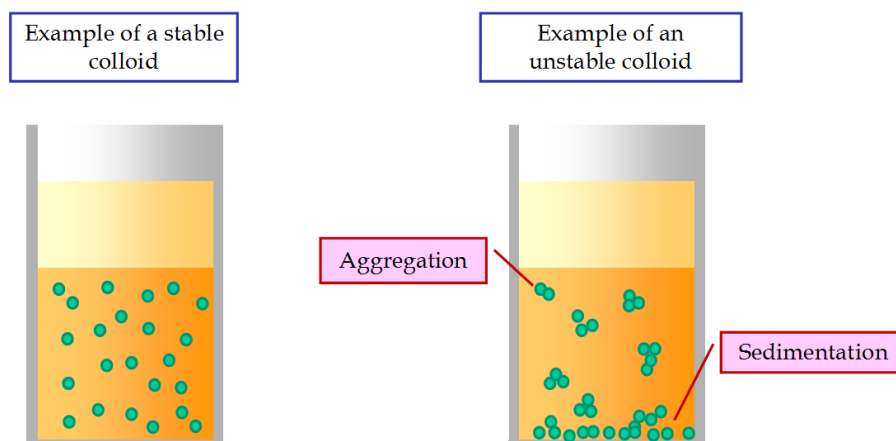
Figure 3.2: Examples of a stable and of an unstable colloidal dispersion [57].

directly affects this sedimentation time. The objective is to obtain more stable suspensions to obtain more homogeneous and adhered screens. To this end, it is also important to maintain the particles separated between them while they are in the suspension with the use of a deflocculant (sodium docusate, see section 3.1.1). The stability of the colloidal suspension is key to obtain better properties on the final screens. This is explained in the following.

Stabilization

The stability of a colloidal system is defined by particles remaining suspended in solution and depends on the interaction forces between the particles. These include electrostatic interactions [54].

A colloid is stable if the interaction energy due to attractive forces between the colloidal particles is less than $k_B T$, where k_B is the Boltzmann constant and T is the absolute temperature. If this is the case, then the colloidal particles will repel or only weakly attract each other, and the substance will remain a suspension. If the interaction energy is greater than $k_B T$, the attractive forces will prevail, and the colloidal particles will begin to clump together. This process is referred to as flocculation [55]. Flocculation describes reversible aggregation involving weaker attractive forces, where the forces holding the particles together are not stronger than external forces caused by stirring or mixing. The objetive is to minimize flocculation in order to obtain suspensions more stable that will sedimentate in a more homogeneous way. The term sedimentation is normally reserved for describing a phase change from a colloid dispersion to a solid (sediment) [56].

3.1.3 New methodology

To obtain more stable suspensions some changes in the mixture process are made. Instead of putting the powders inside the whole quantity of water, the process is done backwards: the powders are put on a tray (see figure 3.7b) while a few drops of water are added. With a dipstick the powders are mixed with the water while more water is added. When a concentrated mixture is obtained, it is moved to the beaker with the magnetic stirrer. While stirring, more water is slowly added until the necessary quantity of distilled water is inside. In that way, a better stability is obtained, and the phases (phosphor and water) remain together when the stirrer stops.

The deflocculant is diluted in 2 ml of water separately, while heated to improve the dilution. Once it is completely diluted, it is added to the phosphor suspension.

To deposit the mixture on the plate, instead of covering the whole petri dish with the suspension, just the stainless steel plate is covered. The quantity of mixture deposited is adjusted so that the surface tension makes the liquid cover just the plate (see figure 3.3c). By using surface tension, more homogeneity is aimed, as the irregularities (the borders) of the plates are avoided.

24 hours after the deposition, the phosphor is completed deposited on the plate, while the water that does not evaporate remains on the plate, but as a separate phase. The step of drying previously explained in section 3.1.1 implies the use of a pipette to remove part of this water. By using surface tension, is not possible to do it as the pipette breaks the tension and the screen breaks down. Because of that, the deposition is made on a laboratory hood, so the wet plate is not moved or touched, while the air current allows a faster drying process.

By the application of these modifications robustness, a higher robustness, adherence and homogeneity is obtained. Several plates have been deposited in this way, as shown in the next section.

Nuclear fusion facilities

The deposition technique explained in the previous section was used to prepare several scintillator screens for the diagnostics explained in section 1.4, for the fusion reactors ASDEX Upgrade (Germany) and DIII-D (USA). The final results of the scintillator plates and its installation in the different diagnostics are shown in the following figures: in the ASDEX Upgrade reactor, FILD diagnostics scintillators in figure 3.4, INPA diagnostic in figure 3.5 and i-HIBP in figure 3.6, while for the DIII-D reactor several scintillator screens
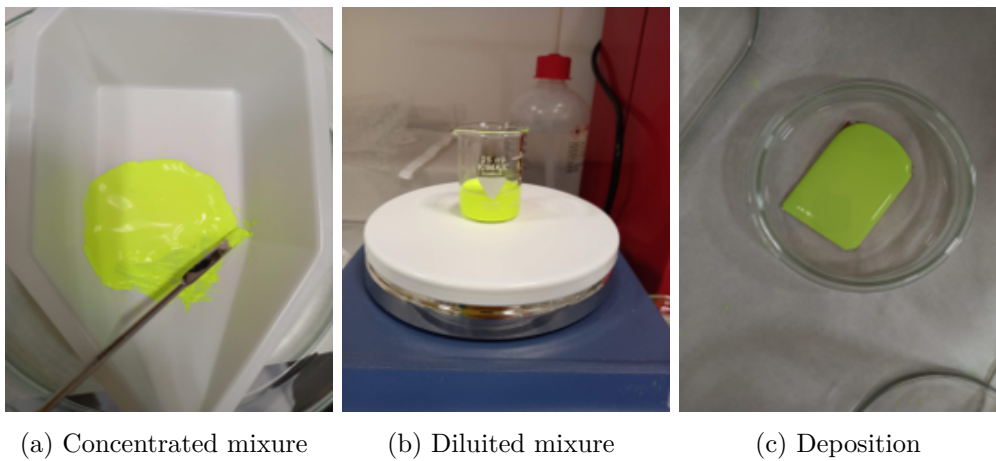
(a) Concentrated mixure   (b) Diluited mixure   (c) Deposition

Figure 3.3: Deposition process at CNA.

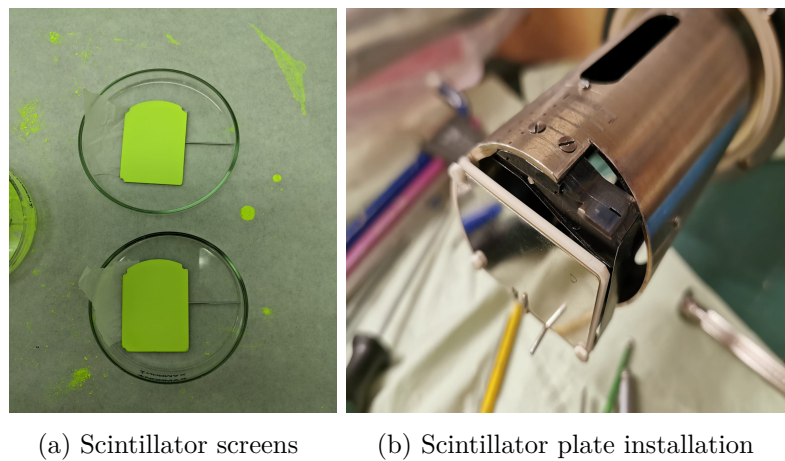(a) Scintillator screens   (b) Scintillator plate installation

Figure 3.4: Plates for a FILD diagnostic at ASDEX Upgrade Tokamak.

have been deposited for a FILD diagnostic (see figure 3.7) and for an INPA diagnostic (see figure 3.8).

An image (figure 3.9) of one of the scintillation screens produced in this work is shown while it is emitting in the i-HIBP diagnostic during an experimental campaign at AUG (reference of the experiment $\#39810@t = 0.217s$). At figure 3.9 the scintillator emission is shown in red.

(a) Scintillator screen

(b) Installed diagnostic
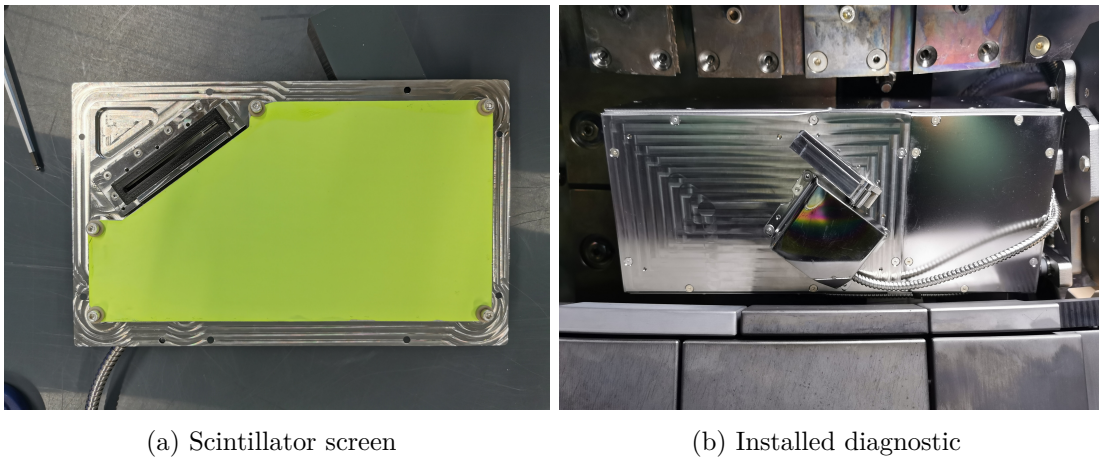
Figure 3.5: Plates for an INPA diagnostic at ASDEX Upgrade Tokamak.

(a) Scintillator screen
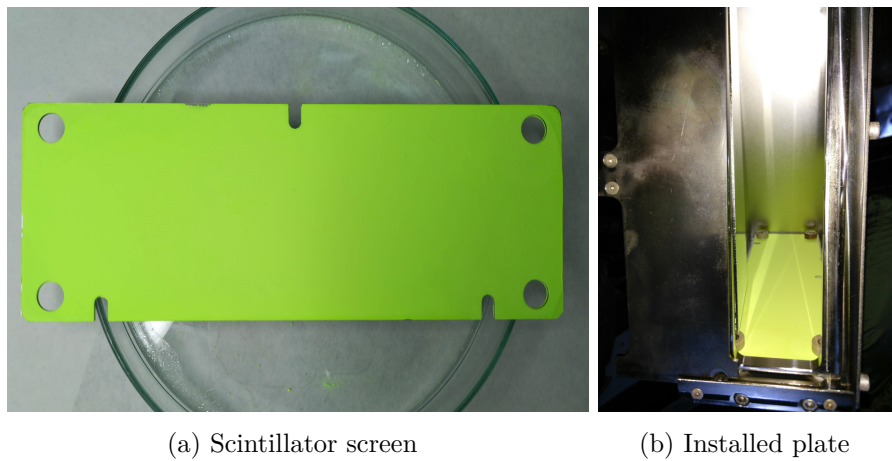
(b) Installed plate

Figure 3.6: Plates for i-HIBP diagnostic at ASDEX Upgrade Tokamak.

(a) Scintillator screen
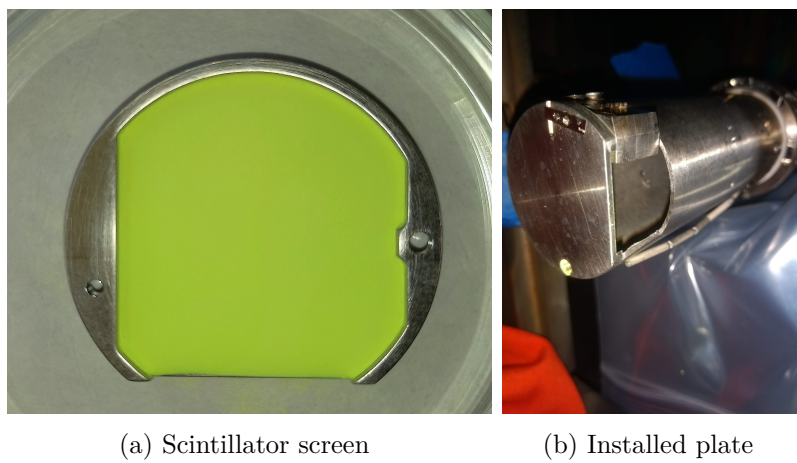
(b) Installed plate

Figure 3.7: Plates for a FILD diagnostic at DIII-D Tokamak.

(a) Scintillator screen   (b) Installed diagnostic

Figure 3.8: Plates for an INPA diagnostic at DIII-D Tokamak.

Figure 3.9: Signal emission of the scintillator plate installed in the i-HIBP diagnostic during real operation.

3.2 Deposition technique at the department of Material Science
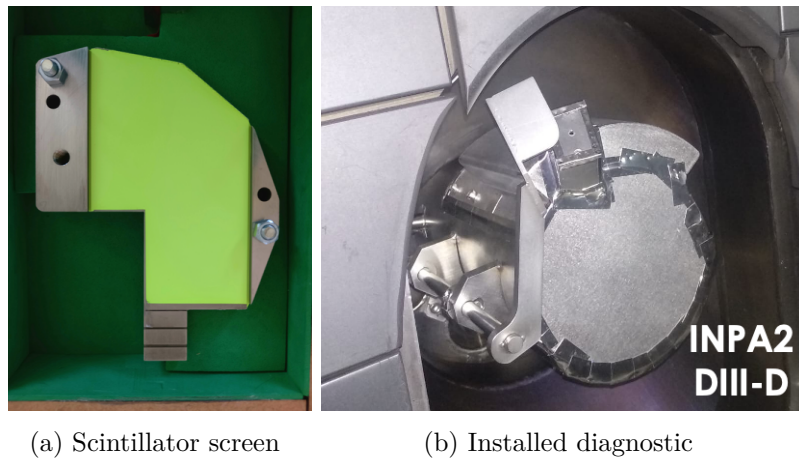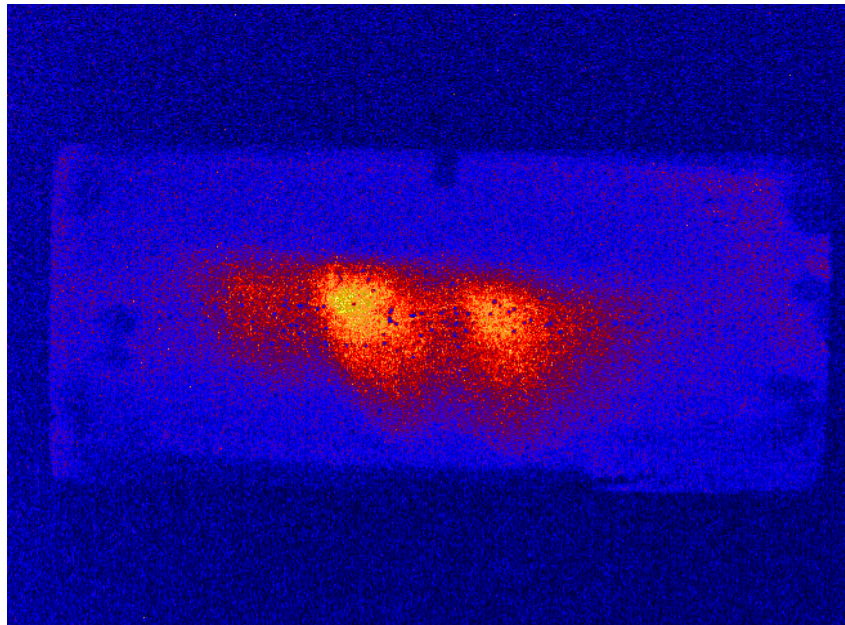
The deposition of the samples that are studied in the present work have been performed in collaboration with the department of Material Science at University of Seville [58]. The same objectives as explained before are followed, with the aim to obtain even more stability with the study of the zeta potential, that is introduced in the next section.

3.2.1 Theoretical background

Zeta potential

Electrostatic stabilization is one of the main mechanisms for stabilization against flocculation. It is based on the mutual repulsion of like electrical charges. Particles in a suspension have a physical property called zeta potential, which measures the charge attraction or repulsion between the particles. If the zeta potential is positive or negative, it means that the particles have a positive or a negative net charge, respectively, and therefore they repeal each other. If the zeta potential is equal to zero, the net charge is zero, and the positive and the negative particles will tend to agglomerate. It is important to avoid a zero value of the zeta potential and tend to an extreme value, either positive or negative. The main parameter that affects the zeta potential is the pH of the mixture. By varying the pH of the colloidal dispersion and measuring the zeta potential, it is known which values of the pH favor that the particles remains separated. Knowing this, when preparing the mixture for the deposition, the pH can be easily change to a value that provides positive or negative zeta potential, by adding an acid or base. A zeta potential study of the scintillator materials is carried out in collaboration with the department of Materials Science of the University of Seville. The results for the powders of the different materials (including two TG-Green samples, one manufactured by the enterprise PhosphorTech and the other one by Benjing Yujii) are shown in figure 3.10. It can be seen in some cases that the neutral value of the pH provides high negative values of zeta potential, for example, for the β-sialon powders. In other cases, it is obtain a more negative value if the pH is changed. The changes in pH that were made according to the results are shown at table 3.1.
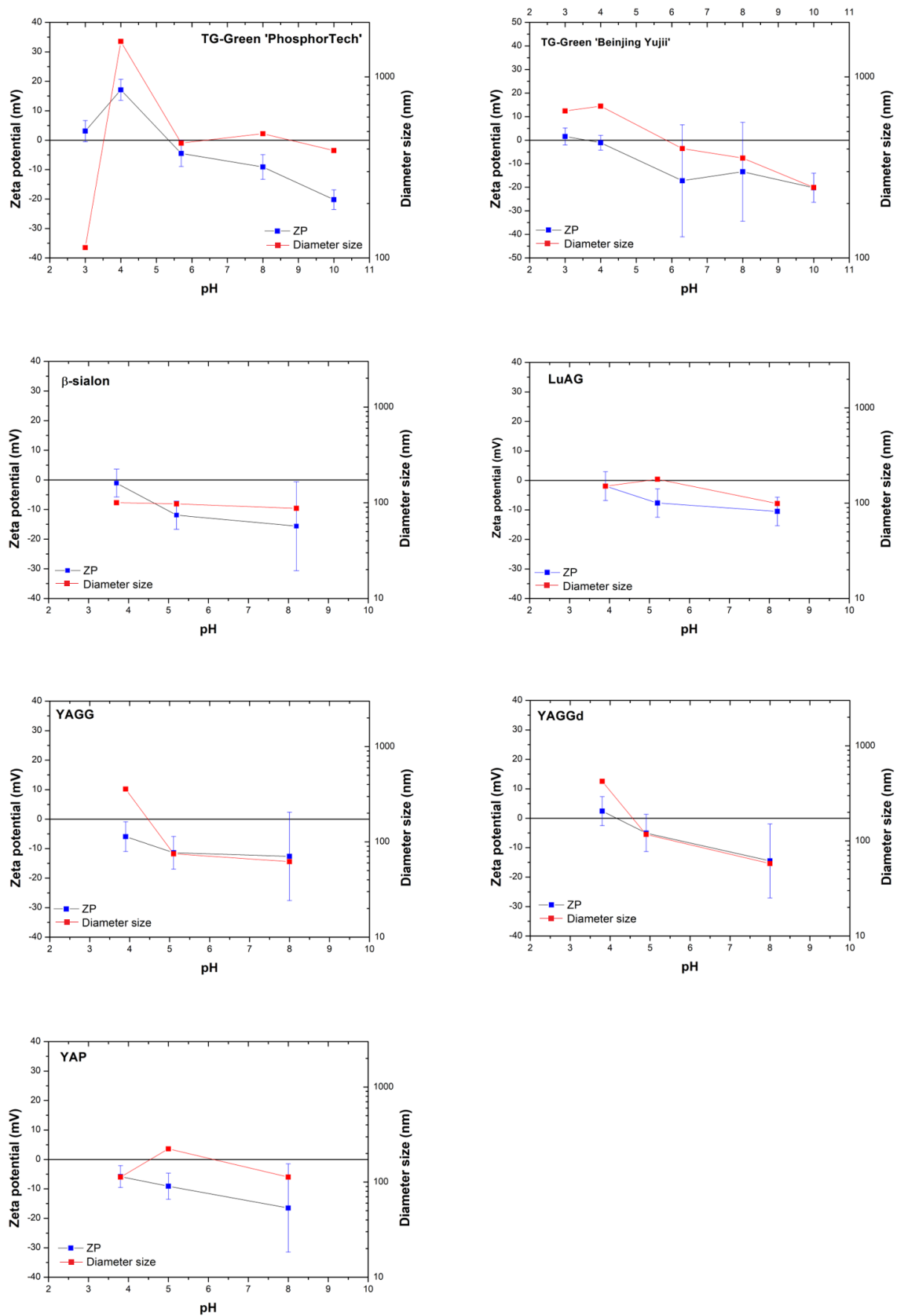
Figure 3.10: Zeta potential results for the different scintillators.

Scintillator	pH
TG-Green 'Beijing Yujii'	10
LuAG	8.2
YAGGd	8.0
YAP	3.8

Table 3.1: pH conditions for the scintillator suspensions.

3.2.2   Methodology

The deposition of the materials using this technique is as follows:

- 1 % m/m deflocculant

- 5 % v/v powders

- 95 % v/v distilled water

Where m/m is percentage by mass and v/v percentage by volume. A suspension with a volume of 3 ml is prepared with each of the scintillation materials under study. The powders and the water are mixed with an ultrasonic transducer, that provides a fast mix with high stability, i.e., the phases do not separate immediately, as with the magnetic stirrer (see section 3.1.1). After that, a pH electrode is introduce into the mixture and, depending on the result that is wanted, few drops of an acid (nitric acid) or a base (caustic soda) 0.1M are added until the pH gets the correct value. Once the pH is adjusted, the deflocculant is added. Its particles link with the separated scintillator particles and isolates them. The suspension is put on the plate with a pipette. The plate is on an incubator that provides a controlled temperature atmosphere of 50ºC.

3.3   Deposition of the samples for the ionoluminescence measurements

To prepare the samples for the ionoluminescence measurements, simulations of the radiation length of the irradiated particles were made, in order to ensure thickness enough of the scintillator screens to completly stop the particles. After that, special plates were prepared for the measurements and the samples were deposited following the technique exposed at section 3.2.2.
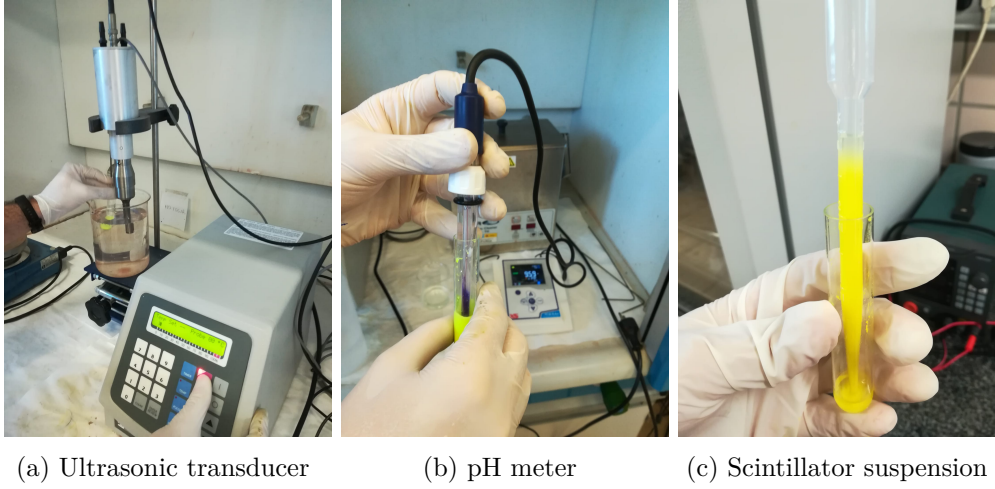
(a) Ultrasonic transducer   (b) pH meter   (c) Scintillator suspension

Figure 3.11: Deposition technique at Material Science Department.

Name	Composition	Density (g/cm^3)	Projected range (μm) alpha 3.5 MeV
P11	ZnS:Ag	4.09	11.26
TG-Green	SrGa$_2$S$_4$:Eu	3.65	12.42
YAP	YAlO$_3$:Ce	5.37	7.57
YAG	Y$_3$Al$_5$O$_{12}$:Ce	4.55	10.01
LuAG	Lu$_3$Al$_5$O$_{12}$:Ce	6.7	7.81
β-sialon	Al$_3$N$_4$Si$_3$O$_4$:Eu	4.01	7.76

Table 3.2: Projected range of the ions of interest into the different scintillation materials.

3.3.1   Stopping power simulations with SRIM

Stopping and Range of Ions in Matter (SRIM) [59] is a computer software which calculate interaction of ions with matter using a quantum mechanical treatment of ion-atom collisions. It is used to calculate the projected range of the incoming ions in the materials under study. Simulations are run for the particles (and energies) that will irradiate the scintillators during the ionoluminescence measurements, that is:

- 3.5 MeV alpha-particles

The input data of the materials is their composition and density (show in table 3.2). The resulting projected range values for each material and radiated particle are recorder in table 3.2 and represented in figure 3.12. As the deeper radiation length simulated is 12.42

μm, the minimum thickness the screen should have is 20 μm. If the real density of the materials is lower than that of the simulations, the project range could be higher, so a margin of several μm is left in the screens to ensure thickness enough to completely stop the particles.

3.3.2   Plate and deposition

With the results obtained in the simulations shown in the previous section, the department Material Science has prepared the plate shown in figure 3.13 for the deposition of the scintillation materials to be subjected to the ionoluminescence measurements. Two different slits have been created to control the thicknesses of the deposited samples, one with a thickness of 50 μm and the second one with 100 μm. For the first time, these slits allow to confirm that the simulated ion beam range is indeed in the mentioned range, as 50 μm should be enough to stop the ions under study, leading to the same efficiency results than the same materials deposited in the 100 μm slit. Once the samples are deposited following the technique exposed in section 3.2.2, the final result is shown in figure 3.14.

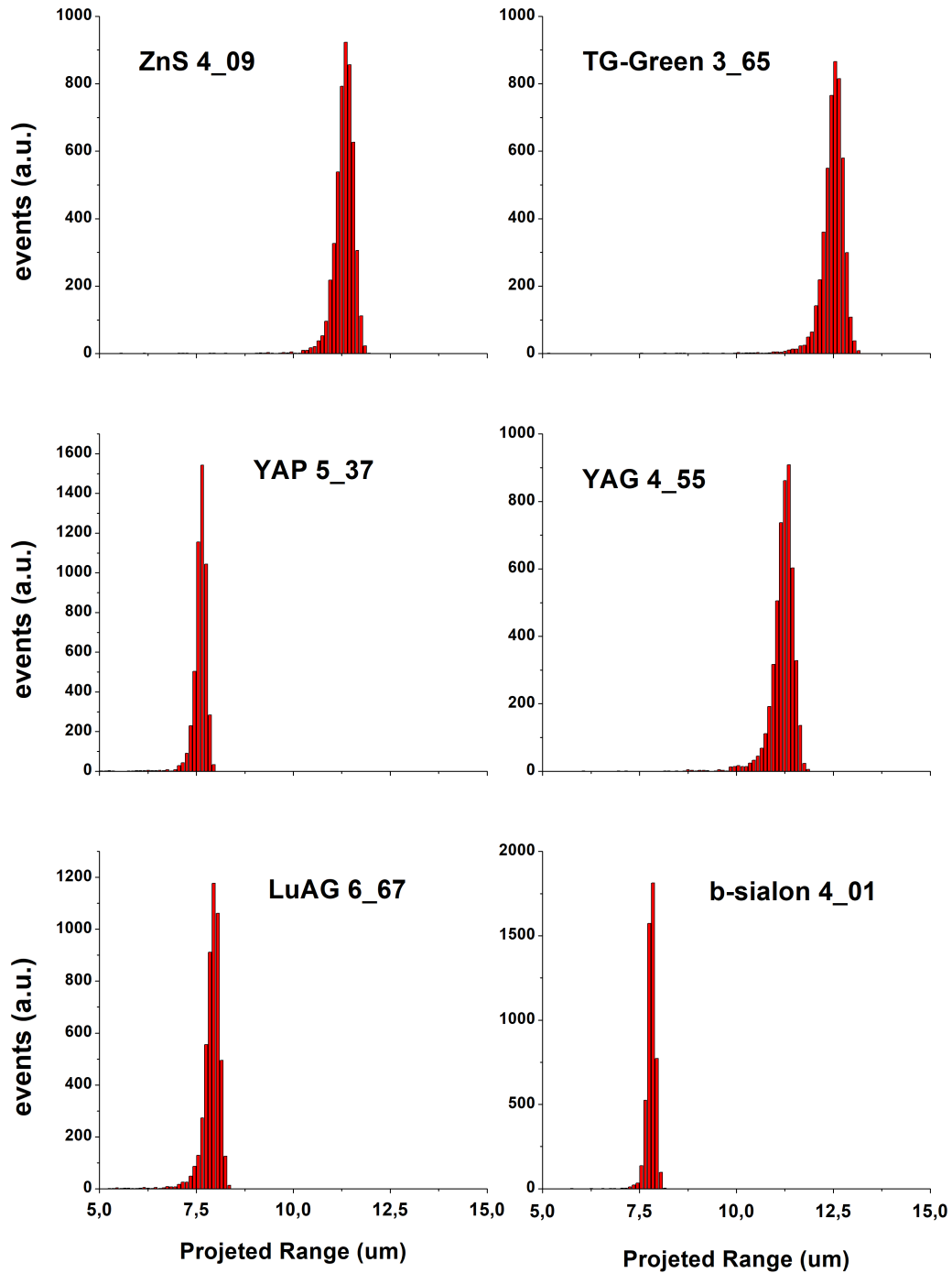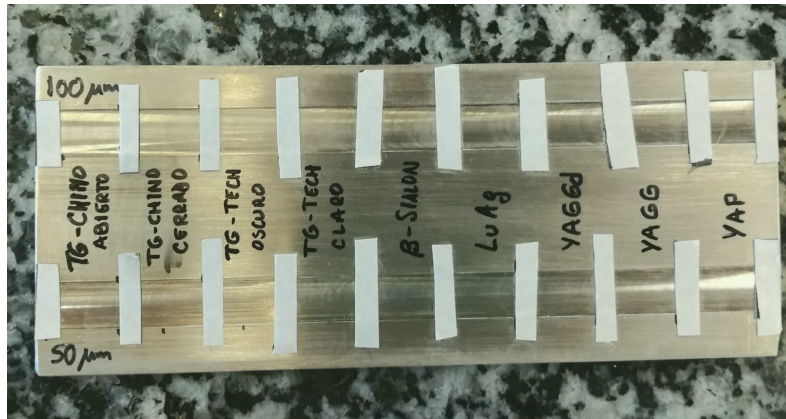Figure 3.12: Projected range of alpha particles of 3.5 MeV in different materials simulated with SRIM code.

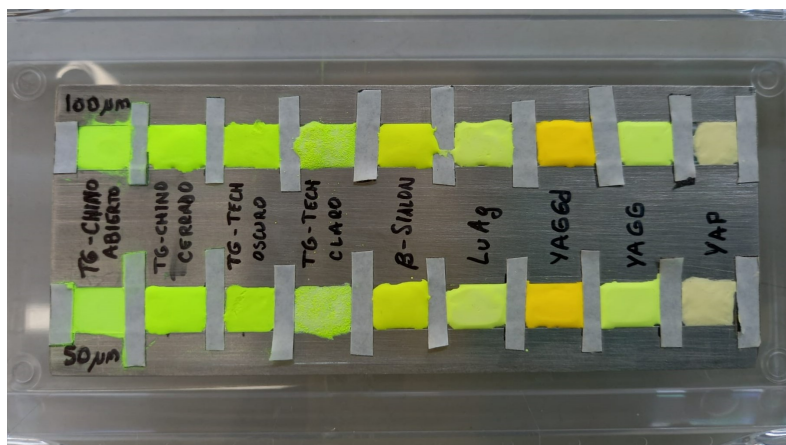Figure 3.13: Plate for the deposition of the scintillators with two slits of 50 and 100 μm.

Figure 3.14: Deposited samples of the scintillators.

Chapter 4

Experimental set up for ionoluminescence measurements

4.1 Tandem accelerator

The characterization of the scintillation screens is done using the Tandem accelerator at the 'Centro Nacional de Aceleradores' (CNA) [60, 61]. The operating principle of this type of accelerators is based on the energy that a charged particle acquires when subject to a potential difference. To achieve the potential difference, a terminal is placed in the center of a steel pressure tank (see figure 4.1). The terminal is an electrode isolated at a high potential. The tension is achieved by a charging chain made up with metal cylinders. A series of gradient rings optimize the transmission of the potential difference along the accelerating tube.

This electrostatic accelerator carry out the acceleration process in two stages. Once the ionic species has been generated by the ion source, they enter the accelerator tank through an injector system (with injection energy $J = eV_{inj}$). The ions are injected with a negative charge state, so that they are attracted to the center of the tank where the terminal is.

Acceleration occurs as a consequence of the potential difference U existing between the tank inlet (which is grounded) and the terminal, which is at a positive potential (up to 3 MV in this accelerator). All the injected ions reach the terminal with the same
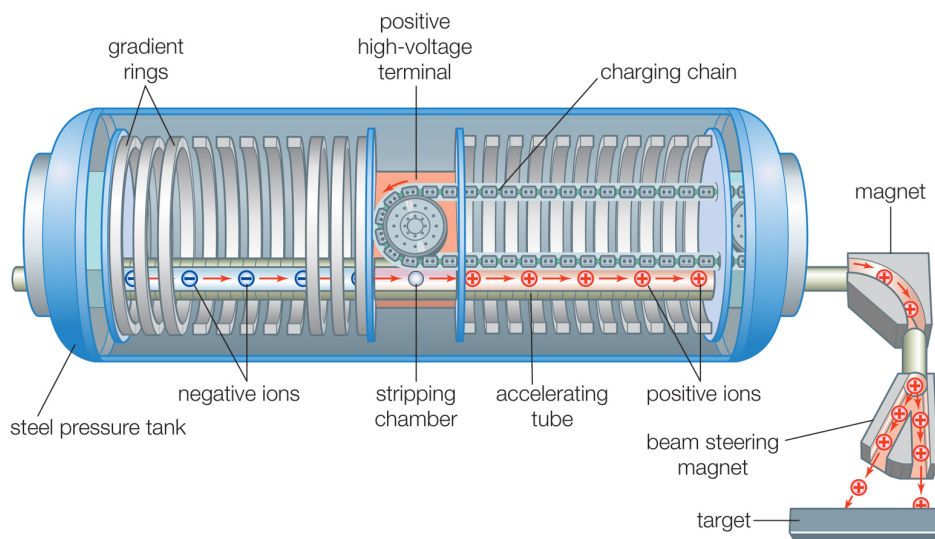
Figure 4.1: Schem of a tandem accelerator.

energy since their charge state is $\eta = -1$. Once the ions have reached the middle of the accelerator tank, they pass through the stripper. The stripper is a narrow tube that contains a residual gas of N_2 at high pressure, in which the accelerated particles interact and transform into positive ions with charge η. These ions leave the acceleration tank after passing through the accelerating tube (second acceleration) because they are repelled by the terminal tension, acquiring an energy $E_2 = \eta eU$. At the end of the acceleration tank, the ions have a final energy given by [39]:

$$E = J + E_1 + E_2 = eV_{inj} + eU + \eta eU = eU(\eta + 1) + eV_{inj} \tag{4.1}$$

Where e is the charge of the electron, U is the working potential of the terminal, η is the positive charge state of the ion in the outlet and eV_{inj} is the injection energy. At the outlet of the tank there are different ions accelerated according to the charge state that the ions acquired in the stripping process. A 90º magnet allows to separate the ionic species and the desired charge state from the rest of the constituents of the beam. In this way, mono-energetic beams are obtained, which are useful for the analysis of materials through different techniques. Finally, the beam can pass directly through the different lines of operation (see figure 4.2) thanks to a steering magnet.
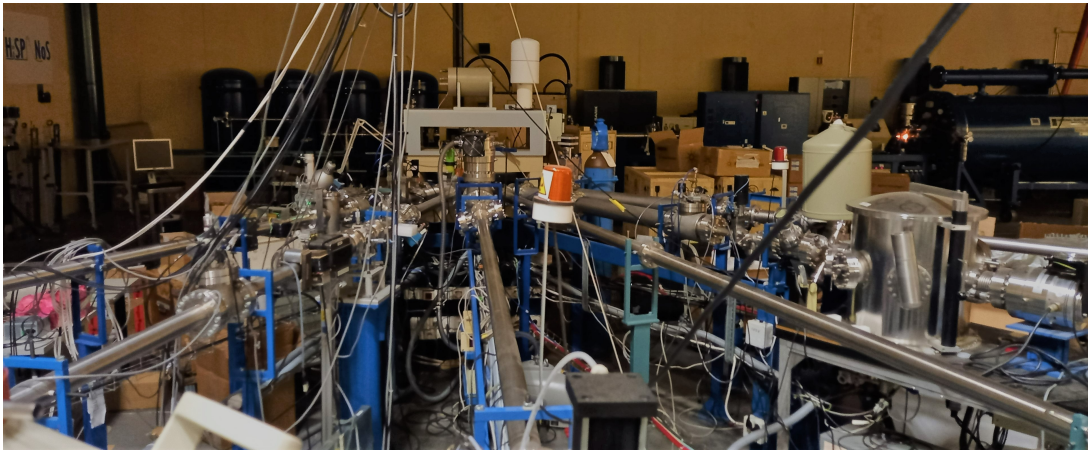
Figure 4.2: Operation lines of the 3 MV tandem accelerator at CNA.

4.2 Experimental set-up

The last element necessary to carry out ionoluminescence measurements with the tandem accelerator consists of a chamber where the samples to be studied are placed. The universal chamber (figure 4.4) is located in the 0º line of the accelerator.

Furthermore, the acquisition system is composed by an optical fiber, a spectrometer and a computer with the corresponding software. In addition, a current integrator measures the intensity of the ion beam. In the following each element of the system is described (figure 4.5) [39, 42]:

- *Universal chamber*

  The universal camera (figure 4.4) is used for different analysis techniques with ion beams. It has a vacuum pump, and a video camera attached that allows real-time monitoring to facilitate the location of the beam on the sample. At the entrance of the chamber there is a collimation system that adjusts the irradiation area with diameters of 0.5, 1 or 3 mm. The rectangular sample holder allows the simultaneous study of several samples. The chamber is electrically isolated. Stepper motors allow the movement of the sample holder along the X-Y directions.

- *Current measurement system*

  In this case, a direct current integration system is used, the sample holder is used as a Faraday cup to know the incident current on the samples. To this end, it is polarized (to +300 V with a voltage source) in order to collect the secondary
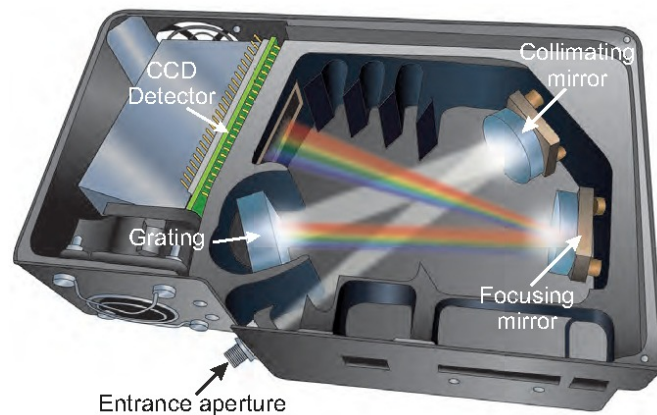
Figure 4.3: Schema of the spectrometer. Extracted from [39].

electrons emitted by the irradiation that could falsify the intensity measurements. A current integrator quantifies the collected current.

- *Optical fiber*

  An optical system is necessary to guide the emitted light from the sample to the spectrometer. In this case, an optical fiber with a diameter of 1 mm is fixed to one of the bushings of the camera at a distance of 22 cm from the sample holder. The fiber collects the emitted photons and it transmits them to the spectrometer for processing and analysis.

- *Spectrometer*

  The optical spectrometer is one of the main elements in the ionoluminescence measurements. The fiber optic cable guides the light to the spectrometer, passing through the entrance aperture (see figure 4.3), the size of which determines the amount of light capable of entering the device, while a filter limits the bandwidth. The light is reflected and collimated by a mirror towards a diffraction grating that disperses the light in the different wavelengths components that constitute it. The light is reflected back by another mirror onto a CCD camera made up of a 2D array of pixels. Each pixel will have a wavelength range. The spectrometer will obtain a spectrum with the number of counts per each wavelength that are recorded for a given acquisition time.

- *Software*

  A computer with a software (Spectrasuite®) is necessary to display and save the spectra registered by the spectrometer.
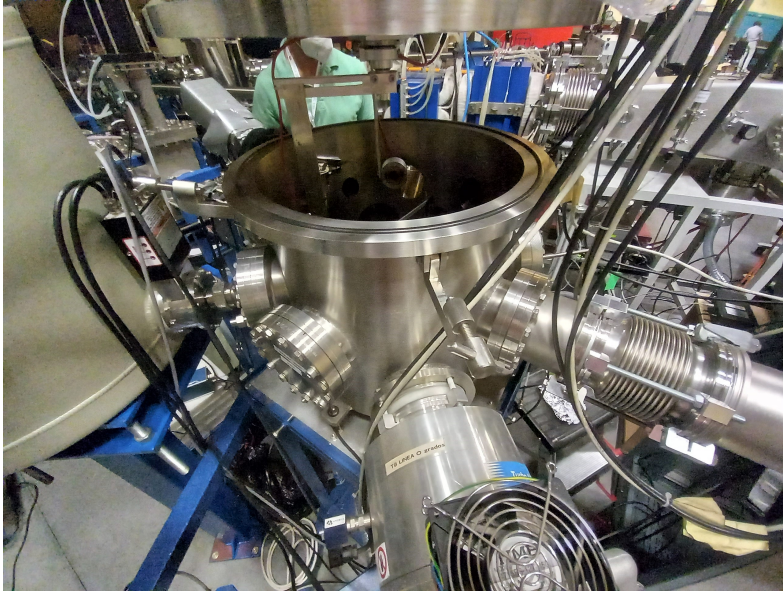
Figure 4.4: Universal chamber.

Calibration of the acquisition system

Since the photons are collected by the optical fiber until they are detected by the computer certain losses occur. The number of photons suffers an attenuation due to different processes, such as the transmission in the optic fiber or the analogical-digital signal conversion. In addition, the number of counts registered in each pixel of the spectrometer detector is not an absolute measurement of the number of incident photons at each wavelength. Therefore, a conversion factor is required for each wavelength so that it transforms the measured spectra (counts) into a spectra given in the absolute number of photons emitted by the sample [39]. For these reasons, the calibration of the optical acquisition system is made using a tungsten halogen lamp (model HL-2000-CAL) that provides tabulated light intensity values. The obtained calibration spectra is shown at figure 4.6.

4.3 Data analysis

The main objective of the ionoluminescence measurements is to obtain the absolute scintillation efficiency, ϵ, of the different materials when irradiated with ions. The scintillation efficiency is defined as the emission rate of photons by the scintillator, $\Gamma_\gamma^{Scintillator}$, divided the incident rate of ions, Γ_{Ions}:

$$\epsilon = \frac{\Gamma_\gamma^{Scintillator}}{\Gamma_{Ions}} = \frac{photons/s}{ions/s} = \frac{photons}{ion} \tag{4.2}$$
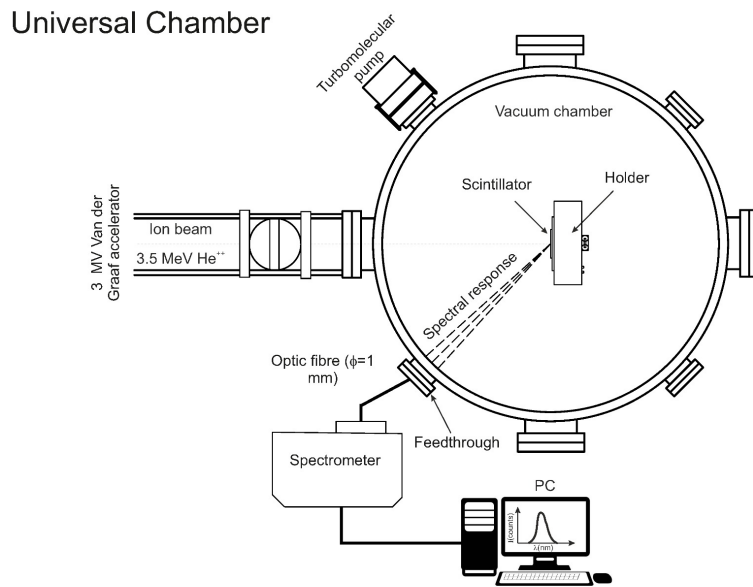
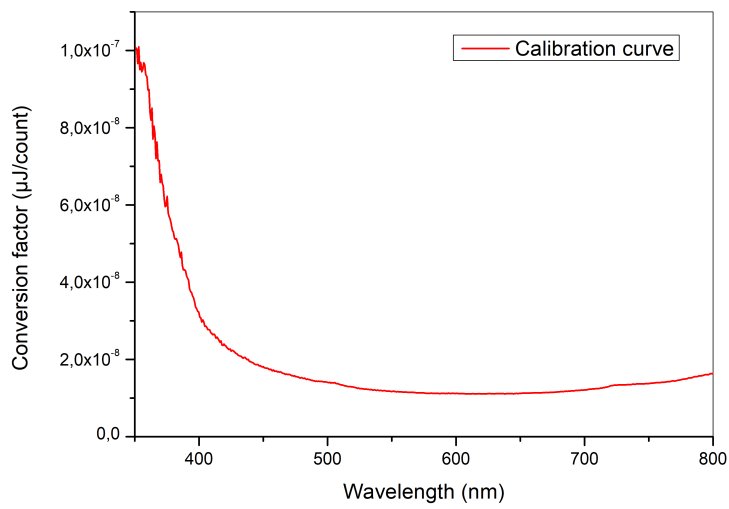Figure 4.5: Experimental set-up. Extracted from [39]

Figure 4.6: Calibration curve.

Photon and ion rates are obtained as follows:

- *Photon rate*

  First, it is necessary to subtract the background from the spectrometer signal, so it does not interfere with the measurements. The spectrometer software subtracts the background from the measured spectra by acquiring a spectrum before starting the irradiation of the sample. Once the spectra are acquired, they are expressed in number of counts per wavelength by the software. The number of counts registered for each wavelength is multiplied by the calibration curve, $C(\lambda)$, transforming digital counts into an energy value. The energy of each photon is $E_\gamma = hc/\lambda$, where h is the Planck constant, c is the speed of light in vacuum and λ is the wavelength of the photon. Therefore, by dividing the total energy recorded for a given wavelength by the value corresponding to the energy of a photon with that wavelength, the number of photons is obtained (registered by the optical fiber, during the acquisition time and for each wavelength). The selected acquisition time, Δt, is 1 second, sso the photon rate per second are known. The expression of the emission rate is:

  $$\Gamma_\gamma(\lambda) = \frac{\lambda \cdot C(\lambda) \cdot N(\lambda)}{\Delta t \cdot h \cdot c} \tag{4.3}$$

  where $N(\lambda)$ is the number of counts registered for each wavelength. Once the units of the spectrum are transformed into photons/s, it is necessary to choose a region of interest (ROI) of wavelengths with the emission of interest. By integrating the emission rate in the whole ROI range, the total number of photons per second that have reached the optical fiber is obtained. Defining the ROI, $[\lambda_1 : \lambda_2]$, the absolute rate of photons/s that have reached the fiber is given by:

  $$\Gamma_\gamma^{fiber} = \sum_{\lambda_1}^{\lambda_2} \Gamma_\gamma(\lambda) \tag{4.4}$$

  The optical fiber only collects the photons emitted at the solid angle supported by its entrance, with respect to the whole irradiation area of the scintillator material. Assuming that the scintillator emits isotropically, the total number of photons emitted by the scintillator per second is:

  $$\Gamma_\gamma^{Scintillator} = \frac{4\pi}{\Omega} \times \Gamma_\gamma^{fiber} = \frac{4\pi d^2}{S} \times \Gamma_\gamma^{fiber} \tag{4.5}$$

Where Ω is the solid angle that is calculated as the section of the optical fiber, S, with a diameter of 1 mm, divided by the square of the distance to the scintillator material, d^2, with d=22 cm.

This calculation is made for every spectrum recorded by the spectrometer (approximately 30 seconds of irradiation per sample), being the final emission rate of each scintillator the average rate of the considered spectra.

- *Ion rate*

  The intensity of the beam is recorded by the current integrator, given in tens of nC per second. To relate each intensity value to the corresponding spectrum both the intensity and the maximum of the spectra are normalized. A cross-correlation is made between them by an adjustment of their maxima. Only the points in which the difference between the normalized current and the normalized spectrum differ in less than 20% are considered as valid points to calculate the efficiencies. Dividing the beam intensity (charge) per second by the charge of the ion species, the number of incident ions is obtained:

$$\Gamma_{Ions} = \frac{Beam\ charge/s}{Ion\ charge} = \frac{Ions}{s} \tag{4.6}$$

4.4 Measurements

Two different sets of ionoluminescence measurements have been done, even though just the α-particles results are shown in the present work. The following ion sources and energies have been used:

- 3.5 MeV α-particles, in order to study fusion born particles in ITER [62] (see section 2.2.1), in the 100 μm samples.

- 1 MeV protons (ITER conditions [62]) measurements in 50 μm and 100 μm, in order to prove that 50 μm is enough to completely stop the incident particles, as simulated with the code SRIM (see section 3.3.1).

Chapter 5

Results

5.1 TG-Green samples

As explained in section 2.2 five different scintillation materials are analyzed by means of ionoluminescent measurements in order to compare their scintillation efficiencies with the current used scintillator, TG-Green. The samples are deposited as explained in section 3.3, but, as shown in figure 3.14 four different samples of TG-Green have been deposited. As described in chapter 2, the challenge with the TG-Green scintillator is its low commercial availability. The PSFT group has purchased the last TG-Green powders available on the market, one from the manufacturer 'PhosphorTech' and the other from 'Beijing Yuji'. Two different samples are analyzed of each manufacture. In the case of the TG-Green powders made by 'Beijing Yuji', samples from two different bottles (from a visual inspection they appear equal) are studied. One of the bottles was opened a year ago, and suffered decomposition due to the contact with air. The decomposition is appreciated as sulfur is part of the TG-Green composition and can decompose into sulfur oxide, associated to a characteristic smell. Furthermore, humidity is appreciated in the powders that were open a time ago. The second bottle was opened in the moment the sample was deposited in order to compare both samples and obtain information about a possible degradation of the powders and its effect on the efficiency. Furthermore, two different samples are deposited with powders manufactured by 'PhosphorTech' from two different bottles, that have been bought in 2018 and 2021 and show a difference in the intensity of the colour, that could be explained by a difference in the grain size, as it is manufactured discontinuously. In order to test if this affects the efficiency, both powders are studied

Scintillator	Manufacturer	Characteristic property
TG-Green 1	Beijing Yuji	'Opened' bottle
TG-Green 2	Beijing Yuji	'Closed' bottle
TG-Green 3	PhosphorTech	'Dark' colour
TG-Green 4	PhosphorTech	'Light' colour

Table 5.1: Different samples of TG-Green.
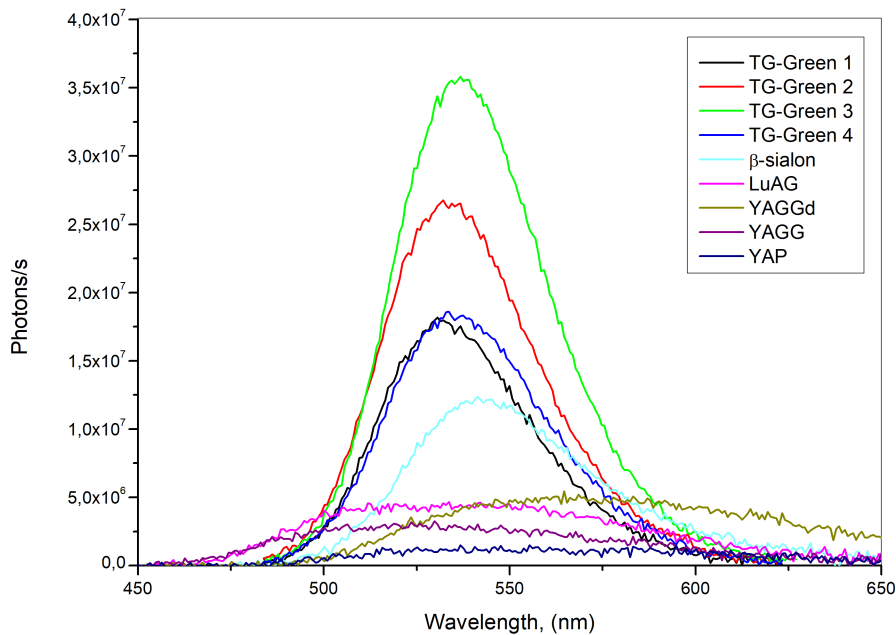
Figure 5.1: Spectral response of the scintillators.

with ionoluminescence measurements. To differentiate the samples made with different bottles of TG-Green, the nomenclature shown in table 5.1 is used.

5.2 Spectral response

When irradiated with the ion beam (3.5 MeV alphas) the samples emit photons that are recorded as counts by the acquisition system. The resulting spectra, in absolute number of photons per wavelength are shown in figure 5.1. The regions of interest (ROIs) and peak emission of the samples are shown in at table 5.2.

Scintillator	ROI (nm)	Peak emission (nm)
TG-Green 1	483.75-623.25	530
TG-Green 2	483.75-623.25	532.07
TG-Green 3	483.75-623.25	536.73
TG-Green 4	483.75-623.25	533.62
β-sialon	475.39-707.3	542.16
LuAG	452.44-707.3	533.62
YAGGd	452.44-707.3	564.64
YAGG	436.74-669.98	529.73
YAP	350.73-692.09	536.73

Table 5.2: Region of Interest (ROI) and peak emission of the analysed materials.

5.3   Absolute efficiency

During the measurements, the α-particles source fluctuates, so the photon emission of the scintillator should fluctuate as well. Nevertheless, this tendency is not observed for every measurement. A cross-correlation have been done between the normalized current gave by the counter (see section 4.3) and the normalization of the ROI of the spectra. The result is shown in figure 5.2.

As it is shown, some of the points highly differ from the counter to the spectrum, even a zero current measurement is registered in the case of YAGGd. It can not be a variation of the real current, but a bad measure of the current, that can be due to a discharge in the scintillator screen. For this reason, a selection criterion is taken, in order to avoid wrong measurements. The selection criterion considers only values which differ less than the 20% between the counter and the spectrum.

By following the data analysis explained at section 4.3 the ionoluminescence efficiencies are obtained and recorded at table 5.3 for the samples when irradiated by α-particles 3.5 MeV. These results demonstrate that:

- Amongst the new materials, YAGGd and LuAG have the best efficiencies, of the same order as the efficiency of TG-Green. β-sialon, YAGG and YAP have results with an order of magnitude below TG-Green, YAGGd and LuAG.

- In general, the TG-Green scintillator shows $\sim 50\%$ more efficiency than the best results obtained with the new materials that were tested in this work, released by
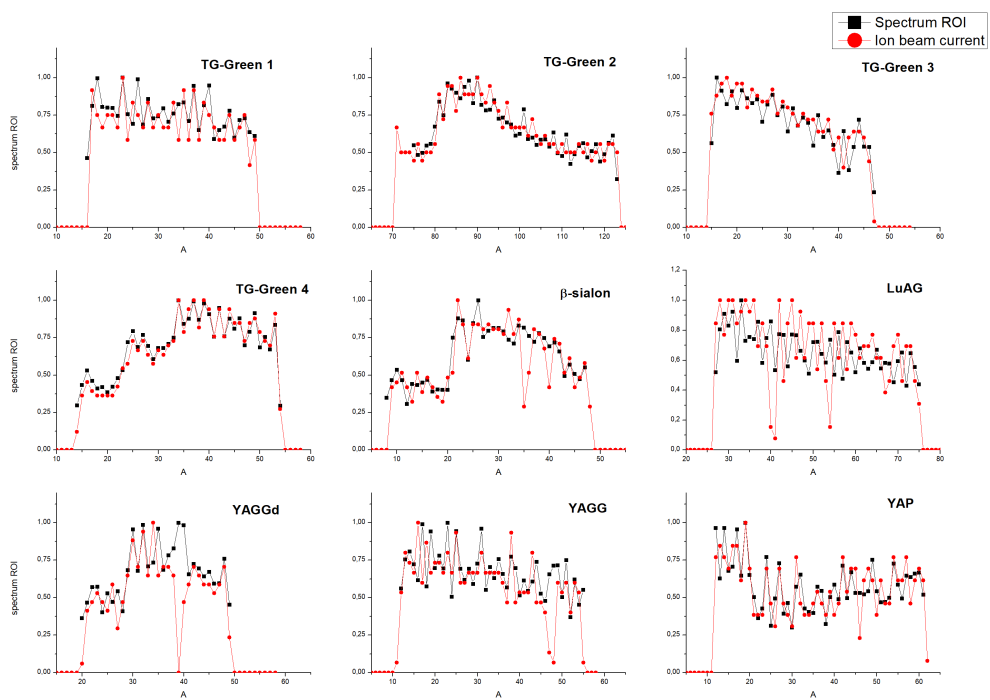
Figure 5.2: Cross-correlation: beam current with correspondent spectra.

Scintillator	Efficiency, ϵ (photons/ion)	Standard deviation, σ (photons/ion)	Relative error, ε (%)
TG-Green 1	$2.60 \cdot 10^5$	$2.82 \cdot 10^4$	10.82
TG-Green 2	$2.50 \cdot 10^5$	$2.90 \cdot 10^4$	11.60
TG-Green 3	$2.32 \cdot 10^5$	$2.57 \cdot 10^4$	11.06
TG-Green 4	$1.01 \cdot 10^5$	$8.30 \cdot 10^3$	8.20
β-sialon	$8.23 \cdot 10^4$	$9.08 \cdot 10^3$	11.03
LuAG	$1.13 \cdot 10^5$	$2.46 \cdot 10^4$	21.83
YAGGd	$1.24 \cdot 10^5$	$1.32 \cdot 10^4$	10.61
YAGG	$7.44 \cdot 10^4$	$1.96 \cdot 10^4$	26.36
YAP	$7.92 \cdot 10^4$	$1.02 \cdot 10^4$	12.85

Table 5.3: Ionoluminescence efficiencies of the scintillators under study.

YAGGd and followed by LuAG.

- The decomposition of TG-Green does not affect the scintillator efficiency. In fact, the 'opened' bottle (TG-Green 1) sample demostrates better results of luminescence than the 'closed' sample (TG-Green 2).

- The colour (grain size) affects the efficiency, as shown by the samples 'dark' (TG-Green 3) and 'light' (TG-Green 4). In fact, even though is the same material with the same composition, the efficiency of TG-Green can decrease by 43.5% due to a smaller grain size. The efficiency of the the TG-Green 4 sample is even lower than LuAG or YAGGd efficiencies.

- The phosphor manufactures by 'Benjing Yuji' show the best ionoluminescence results, compared to the new materials and to the TG-Green made by PhosphorTech.

Chapter 6

Conclusions

The search of different scintillator materials that could be employed in ion diagnostics in nuclear fusion devices showed several commercially available materials with fast decay time (on the order of 500 ns) and with a peak emission in the visible light range are available. The materials selected for testing under ionoluminescence measurements were β-sialon, LuAG, YAGG, YAGGd and YAP. The previously used deposition technique based on sedimentation have been improved at CNA and at the Material Science Department of the University of Seville by improving the stabilization of the suspensions by changing the mixture process. The change in the mixture is beginning with a concentrate mixture that is then diluted and at the Material Science Department by the use of an ultrasonic transducer and the control of the pH of the suspension. Screens with more homogeneity, robustness and adherence were obtained. Furthermore, for the first time the thickness of the screen is controlled with the use a slit in the plate in which the materials are deposited.

Ionoluminescence measurements were performed with all materials, including four different types of TG-Green. The measurements show that, to date, the most efficient one is TG-Green.

Regarding the new materials that were tested, both LuAG and YAGGd shows an efficiency of $\sim 1 \cdot 10^5$, in the same order of magnitude that TG-Green $\sim 2 \cdot 10^5$. Future measurements changing other variables as, for example, the temperature, could give rise to better relative results.

Regarding TG-Green, it was found that its decomposition does not affect its efficiency, its grain size (that also visually changes the colour of the powder with a larger grain size leading to a darker colour) can affect its efficiency (decreasing it by 50%). Thus, a

future study of the same scintillator with different grain size could contribute to specify a grinding process in order to optimize this parameter.

As future work, LuAG and YAGGd will be studied and new mixes of materials are intend to be studied. In addition, to solve the problem of the low commercial availability of TG-Green, the PSFT group is planning to synthesize this material in the laboratory, in collaboration with the Material Science Department, beginning of next year.

Acknowledgements

En primer lugar me gustaría agradecer a Manolo y Eli por darme la oportunidad de trabajar en este proyecto con el que tanto he disfrutado. Trabajar junto a ellos en el PSFT ha sido una experiencia única. Agradecer en especial a Eli, que desde hace tanto tiempo es un modelo a seguir para mí.

A Javier Ferrer, por las horas y dolores de cabeza que ha pasado a mi lado, siempre con dedicación, paciencia y buena predisposición. Solo puedo dar las gracias por todo lo que me ha enseñado.

A Mauri, que ha estado tan presente desde Croacia como si viviera en Triana. Por contestar largo y tendido a las millones de preguntas que le he hecho. Su ayuda ha sido crucial durante todo el desarrollo de este trabajo.

A Javier García, gracias por la comprensión y ayuda con las medidas, sin la cual no habrían salido adelante a tiempo.

A Ranier, Enrnesto y Javier, que me han abierto las puertas de su laboratorio y me han enseñado el maravilloso mundo de la ciencia de los materiales.

A mis compañeros del PSFT, que vuelven divertido el día a día y suponen un gran apoyo dentro y fuera de la oficina.

Bibliography

[1] Roser M., "Our World in Data- The world's energy problem". 2020, URL `https://ourworldindata.org/worlds-energy-problem`.

[2] Jones G.A. & Warner K.J., "The 21st century population-energy-climate nexus". *Energy Policy*, vol. 93, pp. 206–212, 2016.

[3] Blimpo M., Bank W., Dc W. *et al.*, "The Modern Energy Minimum : The case for a new global electricity consumption threshold". pp. 1–15, 2021.

[4] Bp, "Statistical Review of World Energy". Tech. rep., 2020.

[5] "United Nations-World Population Prospects 2019". URL `https://population.un.org/wpp/`.

[6] Gerland P., Raftery A.E., Šev H. *et al.*, "Reports World population stabilization unlikely this century". pp. 1–5, 2014.

[7] Baranes E., Jacqmin J., & Poudou J.C., "Non-renewable and intermittent renewable energy sources: Friends and foes?" *Energy Policy*, vol. 111, no. September, pp. 58–67, 2017, URL `https://doi.org/10.1016/j.enpol.2017.09.018`.

[8] Toschi R., "Nuclear fusion , an energy source". vol. 36, pp. 1–8, 1997.

[9] "IEA- International Energy Agency". URL `https://www.iea.org/`.

[10] Monograph F.N., "Nuclear Fusion : An Energy Source for the Future". Tech. rep.

[11] "IAEA Nuclear Data Services". URL `https://www-nds.iaea.org/`.

[12] EFDA (European Fusion Development Agreement), "Safety and environmental impact of fusion". Tech. Rep. April, 2001.

[13] Eduardo Oliva G., Ortiz Gómez A., & Moral Fernández N., *Curso Básico de Fusión Nuclear.* Sociedad Nuclear Española (sne), 2017.

[14] Kikuchi M., Lackner K., & Tran M.Q., *Fusion Physics.* International Atomic Energy Agency (IAEA), 2012.

[15] van Oost G. & Gonzalez de Vicente S.M., *Fundamentals of Magnetic Fusion Technology.* International Atomic Energy Agency (IAEA), 2021.

[16] Wesson J., *Tokamaks.* Oxford University Press, 3th ed., 2004.

[17] Chen F.F. & Chen F.F., *Introduction to plasma physics and controlled fusion.* Plenum Press, 1984.

[18] "Neutral beam - The system that makes the Tokamak feel small". URL `https://www.iter.org/newsline/-/3254`.

[19] "Heating the plasma - Hi-Tech Hydrogen Plasma". URL `http://plasmahydro.blogspot.com/2011/11/heating-plasma.html`.

[20] Rueda Rueda J., "Development of an Imaging Neutral Particle Analyzer for the ASDEX Upgrade tokamak". pp. 1–5.

[21] Helander P., *Dynamics of fast ions in tokamaks.* Ph.D. thesis, Chalmers University of Technology, 1994.

[22] García-Muoz M., Fahrbach H.U., & Zohm H., "Scintillator based detector for fast-ion losses induced by magnetohydrodynamic instabilities in the ASDEX upgrade tokamak". *Review of Scientific Instruments*, vol. 80, no. 5, 2009.

[23] García-Muñoz M., Jimenez-Rey D., García-Lopez J. *et al.*, "Characterization of scintillator screens for suprathermal ion detection in fusion devices". *Journal of Instrumentation*, vol. 6, no. 4, 2011.

[24] Herrmann A. & Gruber O., "ASDEX Upgrade - Introduction and Overview". In "Fusion Science and Technology", vol. 44, chap. 1, pp. 569–577, Taylor Francis, 2003, URL `https://doi.org/10.13182/FST03-A399`.

[25] Sharma A.S., Limebeer D.J.N., Jaimoukha I.M. *et al.*, "Modeling and control of TCV". *IEEE Transactions on Control Systems Technology*, vol. 13, no. 3, pp. 356–369, 2005.

[26] Tomarchio V., Barabaschi P., Di Pietro E. *et al.*, "Status of the JT-60SA project: An overview on fabrication, assembly and future exploitation". *Fusion Engineering and Design*, vol. 123, pp. 3–10, 2017, URL `https://www.sciencedirect.com/science/article/pii/S0920379617305859`.

[27] Luxon J.L., "A design retrospective of the DIII-D tokamak". *Nuclear Fusion*, vol. 42, no. 5, pp. 614–633, may 2002, URL `https://doi.org/10.1088/0029-5515/42/5/313`.

[28] Rueda Rueda J., *Design and implementation of an imaging neutral particle analyser at the ASDEX Upgrade tokamak*. Master thesis, Universidad de Sevilla, sep 2020.

[29] Galdon-Quiroga J., Rivero-Rodriguez J.F., Garcia-Munoz M. *et al.*, "Conceptual design of a scintillator based Imaging Heavy Ion Beam Probe for the ASDEX Upgrade tokamak". *Journal of Instrumentation*, vol. 12, no. 8, 2017.

[30] Birkenmeier G., Galdon-Quiroga J., Olevskaia V. *et al.*, "Beam modelling and hardware design of an imaging heavy ion beam probe for ASDEX Upgrade". *Journal of Instrumentation*, vol. 14, no. 10, oct 2019.

[31] Happek U., Yen W.M., Electronics E.S. *et al.*, *Physics and Chemistry of Luminescence Materials, W.M. Yen Memorial Symposium*. ECS transactions: Electrochemical Society, Electrochemical Soc., 2009, URL `https://books.google.com.ar/books?id=sPkZlwEACAAJ`.

[32] Martínez Fuentes M.A., *Análisis de iones supratérmicos en el TJ-II con una sonda liminiscente e investigación de sus mejoras instrumentales y métodos físicos*. Phd thesis, Universidad Carlos III de Madrid, oct 2017.

[33] Virk H.S., *Luminescent Materials and Their Applications*. Trans Tech Publications, Limited, Durnten, Switzerland, 2015, URL `http://ebookcentral.proquest.com/lib/uses/detail.action?docID=1953200`.

[34] Lecoq P. & Chao A., *Inorganic Scintillators for Detector Systems*. Springer, 2nd ed., 2006.

[35] Paez C., *Centelladores*. Universidad de Buenos Aires. Departamento de Física, 2017.

[36] Knoll G.F., *Radiation Detection and Measurement*. Wiley, 4th ed., 2018.

[37] Bizarri G., "Scintillation mechanisms of inorganic materials: From crystal characteristics to scintillation properties". *Journal of Crystal Growth*, vol. 312, no. 8, pp. 1213–1215, apr 2010.

[38] Martínez-Fernández G., *Simulación de fotones ópticos en centelleadores inorgánicos: estudio de DETECT2000*. Master thesis, Universidad Complutense de Madrid, sep 2012.

[39] Rodriguez-Ramos M., *Calibración absoluta y aplicación de los detectores de pérdidas de iones rápidos basados en materiales centelleadores para dispositivos de fusión nuclear*. Phd thesis, Universidad de Sevilla, 2017.

[40] Rodríguez-Ramos M., Jiménez-Ramos M.C., García-Muñoz M. *et al.*, "Temperature response of several scintillator materials to light ions". *Nuclear Instruments and Methods in Physics Research, Section B: Beam Interactions with Materials and Atoms*, vol. 403, pp. 7–12, 2017.

[41] Jiménez-Rey D., Zurro B., García G. *et al.*, "Ionoluminescent response of several phosphor screens to keV ions of different masses". *Journal of Applied Physics*, vol. 104, no. 6, 2008.

[42] Toledo J.J., *Deposición y caracterización de materiales centelladores para su utilización en el detector FILD* . Master thesis, Universidad de Sevilla, 2018.

[43] Gratta G., "R D fot the study of new, fast and radiation hard scintillators for calorimetry at LHC/ RD18". Tech. rep., CERN/LHCC 96-19.

[44] Kamada K., Yanagida T., Pejchal J. *et al.*, "Growth and Scintillation Properties of Pr Doped (Gd, Y)(3)(Ga, Al)(5)O-12 Single Crystals". *Journal of Crystal Growth*, vol. 352, pp. 84–87, 2012.

[45] Secu M., Jipa S., Secu C. *et al.*, "Processes involved in the high-temperature thermoluminescence of a Mn2+-doped MgF2 phosphor". *physica status solidi (b)*, vol. 245, pp. 159–162, 2008.

[46] Hull G., Roberts J.J., Kuntz J.D. *et al.*, "Ce-doped single crystal and ceramic garnet for γ-ray detection". *Hard X-Ray and Gamma-Ray Detector Physics IX*, vol. 6706, p. 670617, 2007.

[47] Kada W., Sudić I., Skukan N. *et al.*, "Evaluation of scintillation properties of α- and β-SiAlON phosphors under focused microbeam irradiation using ion-beam-induced luminescence analysis". *Nuclear Instruments and Methods in Physics Research, Section B: Beam Interactions with Materials and Atoms*, vol. 450, no. October 2017, pp. 157–162, 2019.

[48] Parajuli R.K., Kada W., Kawabata S. *et al.*, "Ion-beam-induced luminescence analysis of β-SiAlON:Eu scintillator under focused microbeam irradiation". *Sensors and Materials*, vol. 28, no. 8, pp. 837–844, 2016.

[49] Vi I.C., Brown I.W.M., Ekstrijm T.C. *et al.*, "Ion beam analysis of sialon ceramics". vol. 118, no. 96, pp. 608–612, 1996.

[50] Kingery W.D., Bowen H.K., & Uhlmann D.R., *Introduction to Ceramics*. Wiley, 2nd ed., 1976.

[51] Demidenko V.A., Gorokhova E.I., Khodyuk I.V. *et al.*, "Scintillation properties of ceramics based on zinc oxide". *Radiation Measurements*, vol. 42, no. 4-5, pp. 549–552, 2007.

[52] Gorokhova E.I., Demidenko V.A., Mikhrin S.B. *et al.*, "Luminescence and scintillation properties of Gd 2O 2S: Tb,Ce ceramics". *IEEE Transactions on Nuclear Science*, vol. 52, no. 6, pp. 3129–3132, 2005.

[53] Sim S.M., Keller K.A., & Mah T.I., "Phase formation in yttrium aluminum garnet powders synthesized by chemical methods". *Journal of Materials Science*, vol. 35, no. 3, pp. 713–717, 2000.

[54] Terence Cosgrove, ed., *Colloid Science: Principles, Methods and Applications*. Wiley, 2nd ed., apr 2010.

[55] Slomkowski S., Alemán J.V., Gilbert R.G. *et al.*, "Terminology of polymers and polymerization processes in dispersed systems (IUPAC Recommendations 2011)". *Pure and Applied Chemistry*, vol. 83, no. 12, pp. 2229–2259, 2011, URL `https://doi.org/10.1351/PAC-REC-10-06-03`.

[56] Douglas H Everett, *Basic Principles of Colloid Science*. Royal Society of Chemistry, jan 1988.

[57] "Floculación: reacción, tipos, aplicaciones, ejemplos". URL `https://www.lifeder.com/floculacion/`.

[58] "Metalurgia e Ingeniería de los Materiales". URL `http://www.inciemat.es/`.

[59] Ziegler J.F., Ziegler M.D., & Biersack J.P., "SRIM - The stopping and range of ions in matter (2010)". *Nuclear Instruments and Methods in Physics Research, Section B: Beam Interactions with Materials and Atoms*, vol. 268, no. 11-12, pp. 1818–1823, 2010.

[60] Respaldiza M.A., Ager F.J., Ynsa M.D. *et al.*, *A 3 MV tandem accelerator at Seville The first IBA facility in Spain.* OECD-NEA, Nuclear Energy Agency of the OECD (NEA), 1999, URL `http://inis.iaea.org/search/search.aspx?orig_q=RN:30039582`.

[61] Respaldiza M.A., Ager F.J., Carmona A. *et al.*, "Accelerator-based research activities at "Centro Nacional de Aceleradores", Seville (Spain)". 2008.

[62] Kurki-Suonio T., Asunta O., Hynönen V. *et al.*, *Fast particle losses in ITER.* oct 2008.